The Effect of Interdigitated Channel and Land Dimensions on Flow Cell Performance

Michael R. Gerhardt, [*,a,z] **Andrew A. Wong,** [**] **and Michael J. Aziz** [*]

Harvard John A. Paulson School of Engineering and Applied Sciences, Cambridge, Massachusetts 02138, USA

We demonstrate the effect of varying the channel and land width dimensions of an interdigitated flow field experimentally and through computational modeling. Measured polarization curves (overpotential versus current density) are reported for a symmetric cell with a ferrocyanide-ferricyanide electrolyte in aqueous potassium chloride. A two-dimensional, coupled fluid dynamic and electrochemical model is developed to interpret polarization results from the symmetric cell. This model suggests that stagnant fluid zones above the center lines of the interdigitated channels negatively impact cell performance. A three-dimensional computational fluid dynamic model is used to calculate the pressure drop and power losses associated with flowing fluid through these flow fields. The voltage efficiency of the cell, corrected for pumping power losses, is evaluated and reported as a function of channel and land width to identify high-efficiency flow fields. The implications for the engineering of large-area flow fields are discussed.
 [DOI: 10.1149/2.0471811jes]

Manuscript submitted June 8, 2018; revised manuscript received July 30, 2018. Published August 22, 2018.

Redox flow batteries (RFBs) are promising potential grid-scale energy storage solutions, due in part to their ability to independently scale power output and energy stored.[1,2] A typical RFB comprises two electrolyte tanks and a cell stack. Each electrolyte tank holds one of either the positive electrolyte (posolyte) or negative electrolyte (negolyte). The size of these tanks and composition of the electrolytes determines the energy storage capacity of the battery. During operation, the electrolytes are pumped into a stack of cells, each of which typically consists of an ion-exchange membrane sandwiched between porous electrodes. Each electrolyte is dispersed into the porous electrodes by flow fields, typically made of an inert conductive material such as graphite, with channels to guide fluid and lands to support the porous electrode and provide electrical contact. The design of these flow fields greatly affects flow battery performance by influencing mass transport within the porous electrodes.[3,4] Improving the flow field design has the potential to increase power density and energy efficiency by reducing ohmic losses, mass transport overpotential losses, and pumping power losses, thereby allowing for cost reductions by reducing the cell stack size required to meet rated power targets.

Many flow field designs have been proposed for fuel cells,[5] and several of these are applicable to flow batteries as well. In particular, the use of serpentine or interdigitated flow fields in vanadium redox flow batteries (VRFBs) can result in performance improvements over parallel flow fields.[3,4] Furthermore, computational studies have indicated that, for fixed area-specific flow rate, interdigitated flow fields have lower pressure drops than serpentine flow fields of the same area.[6] Many studies also demonstrate superior polarization performance for interdigitated flow fields,[4,7,8] but some work suggests serpentine flow fields may exhibit higher voltages for a given current.[9] These seemingly contradictory results could be due to the use of different channel and land width specifications in the flow field, and highlight the importance of understanding mass transport in flow batteries as it relates to flow field geometry.

Many computational modeling studies have been performed in attempts to simulate and optimize RFB performance. Most of these studies focus on the vanadium redox flow battery. Shah et al. demonstrated a two-dimensional model of a flow-through VRFB and investigated concentration and current distributions throughout the porous electrodes.[10] The authors later used this model to simulate cycling of a VRFB.[11] Ion and water transport across the membrane was studied in a transient VRFB model by Knehr et al.[12] The Skyllas-Kazacos group has computationally investigated several areas of VRFB stack development, including studying the effect of heat generation[13] and shunt currents.[14,15] Xu et al.[16] investigated the performance of the serpentine, parallel, and flow-through flow fields numerically and compared them on the basis of power and energy efficiency. Topology optimization has been proposed as a method of optimizing porous material placement in complex VRFB flow fields.[17]

Other RFB modeling work studied the bromine electrode, for use in systems including hydrogen-bromine, zinc-bromine, and quinone-bromine batteries. A three-dimensional simulation of a hydrogen-bromine flow battery suggested better polarization performance when using a flow-through flow field on the bromine side rather than a serpentine flow field.[18] Kok et al.[19] studied the effect of altering the geometry of an interdigitated flow field, as well as some properties of the porous electrode, on the peak power density of a bromine electrode such as those used in bromine flow batteries. In the work by Kok et al., the effects of channel width, land width, electrode thickness, electrode porosity, fiber diameter, and exchange current density were studied. Their studies on electrode properties suggest that highly porous electrodes ($\epsilon > 0.85$) with fibers of about 1–2 micrometer diameter will maximize galvanic power density. Furthermore, they found that using small channels (0.5 mm) compared to lands (>1 mm) reduces areas of low utilization in the porous electrode. This paper advances the work by Kok et al. by explicitly including power losses due to pumping, and by increasing the range and resolution of land and channel widths studied. Furthermore, the electrochemical model is validated with experimental data on several flow fields. These additions result in specific recommendations for high-efficiency flow fields.

In this work, we demonstrate the effect of interdigitated flow field structure on the electrochemical and fluid dynamic behavior of flow batteries through the use of symmetric, single-reservoir ferrocyanide-ferricyanide cells. The single-electrode symmetric cell approach greatly reduces the number of independent variables, thereby permitting a comparison of model to experiment with fewer free parameters. Additionally, the symmetric cell approach facilitates cell assembly, operation, and comparison to simulations, because steady-state cell polarization performance is readily achieved due to the minimization of changes in electroactive species concentration in the reservoir. Furthermore, by utilizing a relatively benign potassium chloride electrolyte, this approach allows us to machine flow fields in-house out of commercially available resin-impregnated graphite, enabling a rapid systematic study of flow field designs.

Experimentally observed differences between flow field designs can be explained by a two-dimensional finite-element model of a porous electrode including fluid flow, electrochemical reactions, and mass transport. By combining this two-dimensional model with a three-dimensional computational fluid dynamics model, a

*Electrochemical Society Member.
**Electrochemical Society Student Member.
[a]Present address: Lawrence Berkeley National Laboratory, One Cyclotron Road, Berkeley, California 94720, USA.
[z]E-mail: mrgerhardt@lbl.gov

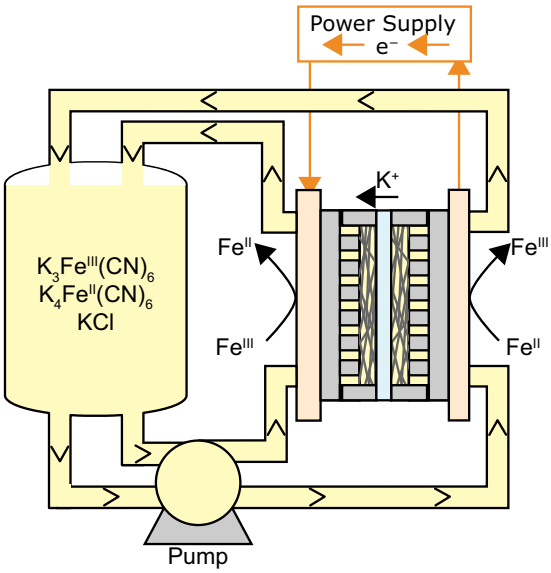

Figure 1. Schematic of the single-reservoir symmetric ferrocyanide-ferricyanide cell used to evaluate various flow fields.

pumping-corrected voltage efficiency is calculated, including power losses due to electrochemical reactions and pumping power losses. These model results suggest a range of channel and land widths over which the pumping-corrected voltage efficiency is effectively maximized. Additionally, this high-efficiency range is not significantly affected by changes in pump efficiency, electrode specific surface area, or electrochemical rate constant for the range of parameters studied. These dimensions properly optimize the trade-off between electrochemical performance gains and pumping power losses due to higher cell pressure drops as land width is increased and channel width is decreased. The paper ends with an analysis of the effects of increasing channel length to industrial scales while simultaneously accounting for changes in channel and land width. By recasting available analytical models for pressure drop in terms of area-specific flow rate, we are able to make specific recommendations regarding scale-up to large-area flow fields without the computational cost associated with full three-dimensional simulations.

Methods

All electrochemical experiments, including polarization curves, were performed using a Gamry Reference 3000 potentiostat. Flow rate and pressure data were recorded using the auxiliary electrometer inputs on the potentiostat. All computations were performed using COMSOL 5.2a (see Supplemental Information for more details on computational methods).

Single-reservoir symmetric ferrocyanide-ferricyanide cell.—To systematically evaluate interdigitated flow fields with varying land and channel widths, a single-reservoir symmetric ferrocyanide-ferricyanide cell was used (Figure 1). This cell circulates an electrolyte solution of potassium ferrocyanide, potassium ferricyanide, and potassium chloride through both the positive and negative electrodes of a standard flow battery. The open circuit voltage of such a cell is zero, so any voltage measured upon applying a current to the cell represents an overpotential. The cell itself consists of a Nafion 212 membrane with one sheet of Sigracet 39-AA (SGL Group, 280 μm uncompressed), cut to 5 cm^2, on each side of the membrane. The Sigracet 39-AA sheets served as the porous electrodes and were pretreated by heating in air at 400°C for 24 hours. Membranes were pretreated by heating in deionized water at 80°C for 1 hour, followed by soaking in 1 M potassium chloride for at least 24 hours prior to use. Polytetrafluoroethylene (PTFE) gaskets of 0.008 inch thickness surrounded each electrode, and a gasket of 0.002 inch thickness provided a seal around the membrane. Flow fields were machined from phenolic resin impregnated graphite (Graphtek LLC) via CNC (computer numerical control) milling, allowing for an accuracy of ±0.025 mm (±0.001 inch) on land width, channel width, and channel depth. All flow fields had an active area of 5 cm^2, determined by the electrode geometric area. Channel and land dimensions for all flow fields are given in Table I and schematics are shown in Figure 2. The cell assembly, including flow plates, was clamped together using aluminum end plates with six 3/8"-24 bolts tightened to 90 inch-lbs torque. The electrolyte was contained in a PTFE reservoir (Savillex) and circulated through perfluoroalkoxy (PFA) tubing (McMaster-Carr) by a dual-channel Cole-Parmer peristaltic pump.

Table I. Channel and land widths of constructed flow fields. The active area in all cases is 5 cm^2. "Contact area" is the total land area facing the electrode.

Name	Channel Width (mm)	Land Width (mm)	Channel Depth (mm)	Contact Area (cm^2)
Micro-channel	0.25	0.79	0.25	2.90
Equal	0.79	0.79	1.90	2.04
Wide Channel	1.59	0.79	1.90	1.47
Extra-wide Channel	2.38	0.79	1.90	1.19
Wide Land	0.79	1.59	1.90	2.83
Extra-wide Land	0.79	2.38	1.90	3.30
Flow-through	1.59	19.0	1.90	4.91

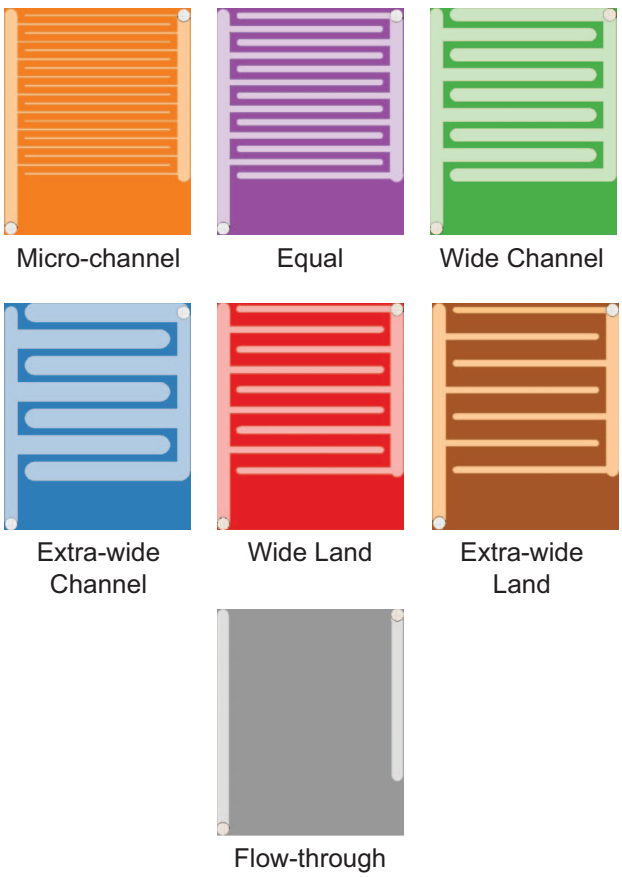

Figure 2. Schematics of the seven constructed flow fields, showing the arrangement of channels (lighter colors) and lands (darker colors) in each flow field. Channel and land dimensions are given in Table I.

Table II. Measured electrolyte conductivities of several ferrocyanide-ferricyanide electrolytes. All electrolytes contain 1 M KCl.

$K_4Fe^{II}(CN)_6$ concentration (M)	$K_3Fe^{III}(CN)_6$ concentration (M)	Conductivity (S/cm)
0.05	0.05	0.13
0.10	0.10	0.15
0.20	0.20	0.21

The flow rate was measured on each side of the cell by an Omega FPR1503 flowmeter. Pressure was measured on the inlet and exit of one side of the cell with Wika 0–15 psi pressure transducers. The pressure transducers were protected from the working fluid with Hayward polypropylene gauge guards.

For each flow field test, a 100 mL electrolyte containing 0.1 M potassium ferrocyanide, 0.1 M potassium ferricyanide, and 1 M potassium chloride was prepared and pumped in parallel through both sides of the single-reservoir cell. The flow rate was adjusted by manually changing the pump rotation rate until the output of the positive-side flowmeter read the desired flow rate. The flow rate and pressure were then recorded for five minutes to ensure stability.

Following the flow rate measurement, potentiostatic electrochemical impedance spectroscopy was performed on the cell at 0 V DC from 100 kHz to 0.1 Hz, with an AC voltage of 15 mV rms. The high-frequency intercept of the real axis of the Nyquist plot was subtracted from each measured polarization curve as an approximate correction for the membrane resistance.[20]

Polarization curves consisted of successive potentiostatic holds from 0.01 to 0.1 V in 0.01 V increments, followed by potentiostatic holds from 0.14 V to 0.5 V in 0.04 V increments. Each potentiostatic hold lasted 30 seconds. Data represent the average current from the final 25 seconds and error bars indicate the full range of measured current at the specified voltage.

Electrolyte conductivity.—Electrolyte conductivity measurements were performed using a custom-built conductivity cell comprising a length of PFA tubing, approximately 8.5 cm long with a 0.125 inch inner diameter and 0.25 inch outer diameter, two T-shaped PVDF push-to-connect fittings, and two 0.25 inch diameter niobium rods for electrodes. Galvanostatic electrochemical impedance spectroscopy was performed using a Gamry Reference 3000 potentiostat, sweeping from 1 MHz to 100 Hz with 0.01 A rms applied AC current (zero DC current). The conductivity cell was calibrated with 1 M and 0.1 M potassium chloride solutions and found to have a length/area (L/A) constant of (109 ± 1) cm^{-1}. Impedances with a phase angle between 2 and −2 degrees near the high-frequency intercept of the Nyquist plot were averaged to calculate the solution resistance. Dividing the cell L/A constant by the resistance gives the electrolyte conductivity.

Conductivity measurements were performed with varying concentrations of potassium ferrocyanide and potassium ferricyanide in 1 M potassium chloride. The high frequency intercepts of the Nyquist plots (Figure S2) were used to calculate electrolyte conductivities as reported in Table II.

Electrolyte viscosity.—Electrolyte viscosity was measured at room temperature ((22.0 ± 0.5)°C) using a ViscoLab 3000 viscometer (Cambridge Applied Systems, Inc.) with a piston for measurements ranging from 0.5 to 10 cP. Approximately 2 mL of 1 M KCl, 0.1 M $K_4Fe^{II}(CN)_6$, and 0.1 M $K_3Fe^{III}(CN)_6$ was loaded into the viscometer chamber for the test.

Measurement of electrode permeability.—In-plane and through-plane electrode permeabilities were measured by a custom testing apparatus following a similar procedure to Feser et al.[21] Circular electrodes, pretreated as described earlier and cut to one inch in diameter, were stacked between two symmetric copper plates with a 0.25 inch diameter center hole and a circular trench having an inner diameter of one inch; these holes and trenches functioned as the fluid inlet and exits. PTFE spacers outside of the circular trench were used to define the compression thickness. In all experiments, deionized water was circulated by gear pump and directed through the apparatus by a series of external valves. Fluid flow rates and pressures were measured by a flowmeter (MicroFlo FTB321D) and pressure gauge (SSI Technologies Inc. MG1-100-A-9V-R) respectively, both at the inlet. The exit flow was returned to an open-air reservoir; therefore exit pressure was assumed to be atmospheric (0 psig). For the through-plane permeability measurements, water entered through one center hole, flowed through the electrode stack, and exited through the opposing center hole. For the in-plane permeability measurements, water entered one center hole, flowed radially through the electrode, and exited through one of the circular trenches; repeated measurements showed that both pressure and flow rate vary only slightly when using either of the two circular trenches as a fluid exit. Through-plane permeability (K_{TP}, in m^2) was calculated by rearranging Darcy's Law,

$$K_{TP} = \frac{-\dot{Q}\mu L_E}{A\Delta P}, \quad [1]$$

where $\dot{Q}$ is the volumetric fluid flow rate, μ is the dynamic viscosity of water, L_E is the compressed stack thickness, A is the cross-sectional flow area, and ΔP is the pressure difference between the fluid exit and inlet. In-plane permeability was calculated by solving Darcy's law for radial fluid flow. Following the work of Feser et al., a radial permeability solution linearized in pressure can be written as

$$K_{IP} = \frac{-\dot{Q}\mu \ln(r_e/r_{in})}{2\pi L_E \Delta P}, \quad [2]$$

where r_e and r_{in} are the exit (0.5 in) and inlet (0.125 in) radii of the permeability apparatus respectively.[21] Inlet flow rate varied between 0 and 200 mL/min and all measured pressures were below 30 psig. The permeability values used in this work assume a compression of 20% (compressed thickness being 80% of the uncompressed thickness) resulting in through-plane and in-plane permeability values of 6.6×10^{-12} m^2 and 1.4×10^{-11} m^2, respectively.

Modeling the Interdigitated Flow Field

The flow battery model presented here consists of two distinct calculations: a two-dimensional, coupled fluid dynamic and electrochemical simulation that computes voltage losses due to the faradaic, Ohmic, and mass transport processes; and a three-dimensional calculation of pressure drop along the channels and through the porous electrode, including only fluid dynamics. A schematic of the two-dimensional model and associated boundary conditions is shown in Figures 3a–3c, and the three-dimensional model with associated fluid flow boundary conditions is shown in Figure 4. The output from these two models is combined to calculate an overall power loss, which is reinterpreted as an effective voltage efficiency.

Modeling fluid flow in porous electrodes and free channels.—A three-dimensional computational fluid dynamics model is used to compute the pressure drop associated with flowing fluid down the inlet channel, up and over the land, and out the exit channel in an interdigitated flow field. Accurate calculation of the fluid velocity field is also important in the two-dimensional voltage loss model, because the fluid velocity strongly influences mass transport and electrochemical performance. In all cases, steady-state, incompressible, laminar flow is assumed, with no external body forces. Therefore, within the channel, the Navier-Stokes equation applies:

$$\rho(v \cdot \nabla)v = -\nabla P + \mu\nabla^2 v, \quad [3]$$

where v represents the fluid velocity, ρ the fluid density, P the pressure, and μ the dynamic viscosity of the fluid.

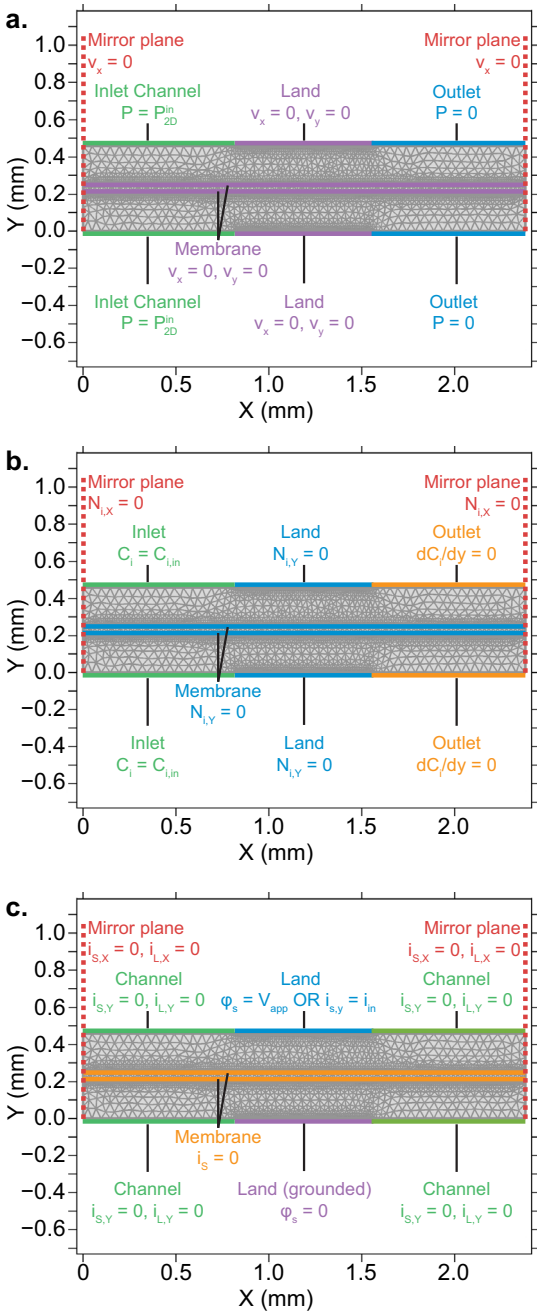

Figure 3. Boundary conditions of the two-dimensional model related to a) fluid flow, b) transport, and c) electrochemical phenomena.

Within the porous electrode, two velocities can be defined: the *volume-averaged* (or *superficial*) velocity v_V, that is the ratio of the volumetric flow rate to the cross-sectional area through which flow is occurring; and the stream velocity $v_S = v_V/\epsilon$, where ϵ is the porosity of the medium. The stream velocity represents the average velocity component in the downstream direction of a fluid element moving through the porous electrode. This velocity is discontinuous at the boundary between the channel and the porous electrode because the porosity is discontinuous. Therefore, for simplicity, we use the volume-averaged velocity v_V throughout the porous electrode and denote it as v because it is continuous with the channel velocity computed by the Navier-Stokes equation. Thus, within the porous electrode, the following modified Darcy's law equation applies:

$$\nabla P = -\frac{\mu}{K} v - \frac{c_F}{\sqrt{K}} \rho |v| v + \mu \nabla^2 v. \qquad [4]$$

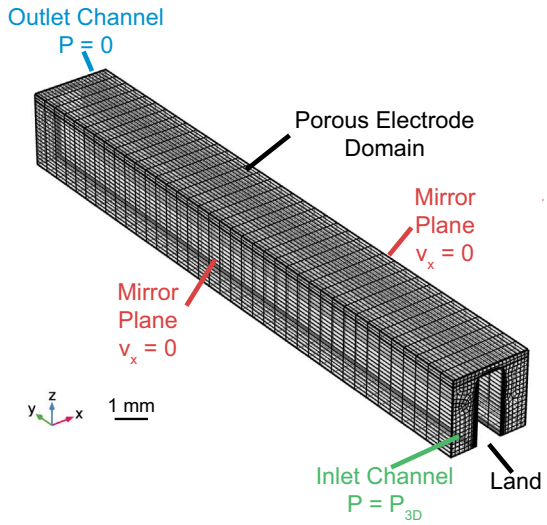

Figure 4. Boundary conditions for the three-dimensional fluid dynamics model. No-slip wall conditions are unlabeled for clarity and apply to every unmarked outer boundary.

The first term on the right-hand side of Equation 4 describes standard Darcy pressure-driven flow, with a dynamic viscosity of μ, and a hydraulic permeability K. The following two terms represent two corrections to Darcy's law that allow more accurate computation of the superficial velocity and pressure.

The second term on the right-hand side of Equation 4 accounts for form drag due to the solid porous material. When the Reynolds number with respect to fiber diameter is greater than 1 in a porous medium, the drag effects become non-negligible, resulting in a non-linear dependence of pressure on fluid flow rate.[22] This phenomenon, known as Forchheimer drag, is observed experimentally as a smooth deviation from linearity in pressure as flow rate is increased through the region $1 < Re < 10$. At high flow rates, the porous electrodes in this work typically cross this Re range. Thus, Forchheimer drag could explain the measured pressure drop increasing above linearity at high flow rate (see, for example, Figure 8). The Forchheimer drag coefficient c_F is assumed to be 0.55.[22]

The third term on the right-hand side of Equation 4 aids in modeling fluid flow behavior close to the no-slip boundaries at the membrane and the electrode surface. Additionally, this term allows Equation 4 to reduce to Stokes flow when $K \to \infty$ and to Darcy's law (with a Forchheimer term correction) as $K \to 0$.[22] Therefore, Equation 4 ensures continuity in the fluid flow solution between the channel and the porous electrode.

Fluid flow boundary conditions.—The boundary conditions for fluid flow in the two-dimensional model are shown graphically in Figure 3a. No-slip boundary conditions are applied along the electrode-membrane interface and the electrode-land interface. The left and right vertical edges of the porous electrode, above the channel center lines, are mirror planes. The boundary between the porous electrode and the inlet half channel is assumed to be an isobar with pressure $P = P^{2D}_{in}$. This pressure is automatically adjusted until a specified average superficial velocity v_{in} is reached across the boundary. This boundary condition allows the superficial velocity to vary with position along the boundary, as long as the average reaches the specified value of v_{in}.

To allow for generalization of our results to larger-area flow fields, we specify an area-specific flow rate, $\dot{Q}_A$, and derive an expression relating it to v_{in}. The desired average superficial velocity v_{in} is related to the total volumetric flow rate $\dot{Q}_T$ and channel/land geometry:

$$v_{in} = \frac{\dot{Q}_T}{N_{C,in} W_C L_C}, \qquad [5]$$

where W_C represents the channel width, L_C is the channel length, and $N_{C,in}$ denotes the number of inlet channels in the flow field. The volumetric flow rate per inlet channel $\dot{Q}_T/N_{C,in}$ can be expressed in terms of the area-specific flow rate $\dot{Q}_A$ by approximating $N_{C,in}$ as $W_{FF}/2(W_C + W_L)$, where W_{FF} and W_L are the total flow field width and land width, respectively, and using the definition $\dot{Q}_A = \dot{Q}_T/W_{FF}L_C$:

$$\frac{\dot{Q}_T}{N_{C,in}} = 2(W_C + W_L)\frac{\dot{Q}_T}{W_{FF}} = 2\dot{Q}_A L_C(W_C + W_L). \quad [6]$$

Equations 5 and 6 can be combined to express v_{in} in terms of $\dot{Q}_A$:

$$v_{in} = \dot{Q}_A \frac{2(W_C + W_L)}{W_C}. \quad [7]$$

At the boundary between the porous electrode and the exit half channel, the fluid pressure is set to zero. In other words, we assume negligible pressure drop through the tubing, manifolding, and any other balance-of-plant components; the effects of additional pressure losses are discussed later.

Extending the fluid flow model to three dimensions.—Boundary conditions for the three-dimensional fluid flow model and an example mesh are shown in Figure 4. Within the channels, the Navier-Stokes equation is solved under the boundary conditions listed below. The inlet boundary of the inlet channel is set as an isobar of pressure $P_{\text{in}}^{\text{3D}}$, that is automatically adjusted until the average volumetric flow rate across the surface reaches the desired value $\dot{Q}_{in}$, calculated as

$$\dot{Q}_{in} = \dot{Q}_T/N_{C,in} = 2\dot{Q}_A L_C(W_C + W_L). \quad [8]$$

This approach matches the average inlet superficial velocity of the two-dimensional model, v_{in}, to the average velocity of the fluid entering the electrode from the channel in the three-dimensional model. The pressure is set to zero at the exit channel boundary. The outer *yz*-planes are mirror planes, while the inner *yz*-planes and the bottom *xy*-planes are no-slip walls.

Within the porous electrode, Equation 4 is solved under the following boundary conditions. The superficial velocity must be continuous across the boundary between the free channel and the porous electrode. The *yz*-edges of the electrode are mirror planes, while the *xz*-edges and *xy*-edges are no-slip walls, save for the portions of the electrode directly above the channels.

Scaling the fluid flow model to long channel lengths.—To scale the pressure drop model to large-area flow fields, we used the analytical model for pressure drop through an interdigitated flow field provided by Darling and Perry,[4] as three-dimensional computational fluid dynamics on long channels proved too computationally expensive. We reproduce the relevant formulae here in terms of $\dot{Q}_A$:

$$\Delta P = \Delta P_{PFF}\left(1 + \frac{2 + 2\cosh\zeta}{\zeta\sinh\zeta}\right), \quad [9]$$

$$\Delta P_{PFF} = \frac{64\mu\,\dot{Q}_A {L_C}^2(W_C + W_L)}{W_C H_C {d_h}^2}, \quad [10]$$

$$\zeta^2 = \frac{128 {L_C}^2 K L_E}{W_L {d_h}^2 W_C H_C}, \quad [11]$$

where d_h is the hydraulic diameter of the channel:

$$d_h = \frac{2W_C H_C}{W_C + H_C}, \quad [12]$$

H_C is the channel depth, and L_E is the thickness of the porous electrode. ΔP_{PFF} represents the pressure drop of a parallel flow field (no dead-ended channels) for the given channel and land dimensions. The pressure drop calculated by Equation 9 approaches ΔP_{PFF} for large values of ζ; that is, the pressure drop becomes dominated by flow down the channel. As ζ approaches zero, and the pressure drop becomes dominated by flow through the electrode, the following limit applies:

$$\Delta P_{\zeta\to 0} = \frac{4\Delta P_{PFF}}{\zeta^2} = \frac{2\dot{Q}_A(W_C + W_L)}{L_E}\frac{\mu W_L}{K}. \quad [13]$$

This limit is also a restatement of Darcy's law, as the term $2\dot{Q}_A(W_C + W_L)/L_E$ is equivalent to the average superficial velocity of fluid flowing across the land.

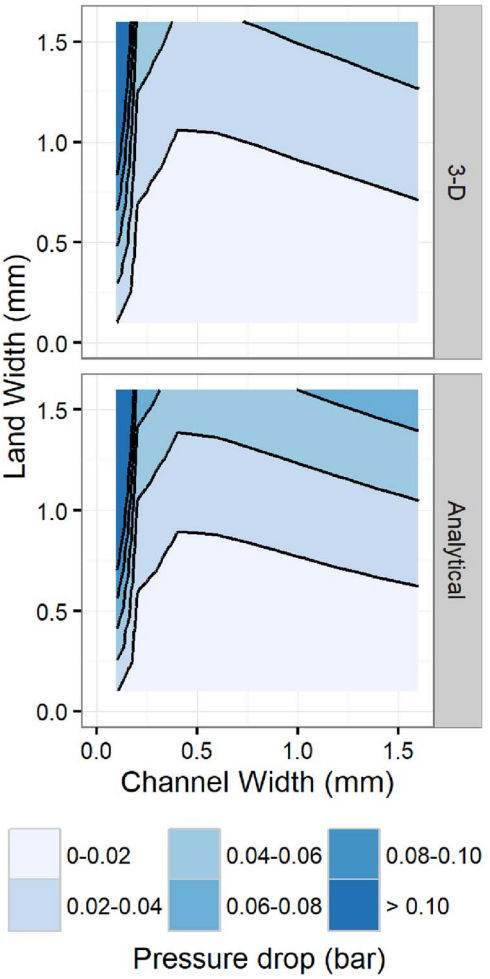

Figure 5. Comparison of pressure drop models for an interdigitated flow field with 2.23 cm channel length at 10 mL min^{-1} cm^{-2}. The analytical model was adapted from Darling and Perry.[4]

Figure 5 illustrates the pressure drop at 10 mL min^{-1} cm^{-2} flow rate for this analytical model and the 3D fluid dynamic model following the grid shown in Figure 6. The analytical model slightly overpredicts pressure drop compared to the 3D model, but well within the error of our flow rate, pressure, and permeability measurements. More importantly, it captures the same features as channel and land width are varied at a fraction of the computational cost.

Modeling mass transport in porous electrodes.—Species are assumed to move throughout the porous electrode via diffusion and convection. The flux N_i of species i throughout the electrode is described by the Nernst-Planck equation:

$$N_i = -D_i\nabla C_i + vC_i, \quad [14]$$

where the electromigration term has been omitted due to the presence of a conductive supporting electrolyte in the experiments. In steady

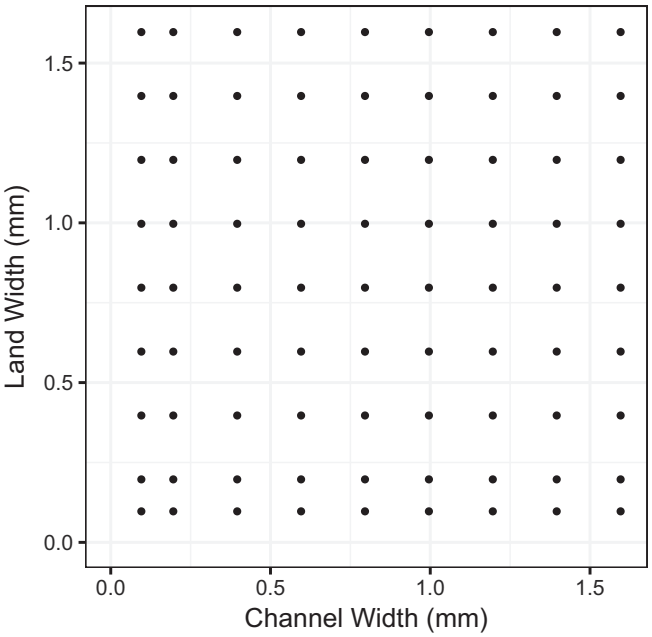

Figure 6. The grid of land and channel widths explored computationally in this work. Each point represents a simulated flow field. Each flow field simulation systematically varied the current density and flow rate.

state, the divergence of the fluxes N_i must be balanced by a species generation term R_i that represents the production or consumption of electroactive species via an electrochemical reaction distributed throughout the porous electrode. This mass balance can be written as:

$$\frac{\partial N_i}{\partial t} = 0 = \nabla \cdot N_i - R_i. \quad [15]$$

The rate of generation or consumption R_i of species i is tied to the rate of the electrochemical reaction that is defined in Equation 20.

Mass transport boundary conditions.—The boundary conditions for mass transport are illustrated in Figure 3b. At the inlet to the porous electrode, the concentration C_i of each species i is set to its initial inlet value $C_{i,in}$. The land and membrane are assumed impermeable, so no-flux boundary conditions are set along both boundaries. At the left and right edges of the model, above the channel center lines, mirror plane boundary conditions are applied. At the channel exit, back-diffusion is suppressed.

Modeling electrochemical reactions and current flow in porous electrodes.—The porous electrode is assumed to be homogeneous, with a porosity ϵ and a surface area per unit volume a. The porous electrode consists of two overlapping, inter-penetrating domains: a solid electron conductor and a liquid electrolyte. Throughout the volume of the electrode, conservation of current applies:

$$\nabla \cdot i = 0. \quad [16]$$

The current density i is apportioned into electronic current in the electrode, i_E, and ionic current in the liquid electrolyte, i_L:

$$i_E + i_L = i. \quad [17]$$

Within each phase, current flows according to Ohm's law:

$$i_E = -\sigma_{eff} \nabla \phi_E, \quad [18a]$$

$$i_L = -\kappa_{eff} \nabla \phi_L, \quad [18b]$$

where ϕ_E and ϕ_L are the electrostatic potentials in the solid (electrode) and liquid (electrolyte) phases, respectively. The porous nature of both the electrode phase and the electrolyte phase results in tortuous conduction pathways, so effective conductivity values are used for each phase. The effective electrode and electrolyte conductivities are given by σ_{eff} and κ_{eff}, respectively. The electrode effective conductivity σ_{eff} can be directly measured via electrochemical impedance spectroscopy on stacks of porous electrodes and is 6.8 S/cm.[20] For the electrolyte, a bulk conductivity κ is measured with a conductivity cell containing an electrolyte conduction path of fixed length and cross-sectional area. This bulk electrolyte conductivity is adjusted to an effective ionic conductivity of the porous electrode by the Bruggeman correction:

$$\kappa_{eff} = \kappa \epsilon^{3/2}. \quad [19]$$

Current is transferred between the two phases by means of a faradaic reaction distributed throughout the porous electrode. The rate of the faradaic reaction can be described by the Butler-Volmer equation:

$$\nabla \cdot i_L = -\nabla \cdot i_E = a i_0 \left[\frac{C_{R,S}}{C_{R,B}} \exp\left(\frac{\alpha n F}{RT} \eta \right) - \frac{C_{O,S}}{C_{O,B}} \exp\left(\frac{-(1-\alpha) n F}{RT} \eta \right) \right], \quad [20]$$

where i_0 represents the exchange current density, a measure of the kinetic feasibility of the electrochemical reaction. The exchange current density is defined as:

$$i_0 = n F k_0 {C_{R,B}}^{\alpha} {C_{O,B}}^{1-\alpha}, \quad [21]$$

where n represents the number of electrons in the electrochemical reaction, F is Faraday's constant, k_0 is the kinetic rate constant of the reaction, and α is the charge transfer coefficient. In Equations 20 and 21, C_O and C_R represent the concentrations of oxidized and reduced species, respectively; and the additional subscripts S and B represent the concentrations at the surface of the porous electrode (edge of a pore) and the bulk of the electrolyte (center of a pore), respectively. The relationship between $C_{O,S}$, $C_{O,B}$, $C_{R,S}$, and $C_{R,B}$ is dictated by a mass transfer coefficient, k_m, defined in Equations 24 and 25. The overpotential η is defined as

$$\eta = \phi_E - \phi_L - E_{eq}, \quad [22]$$

where E_{eq} is the equilibrium value of $\phi_E - \phi_L$, so that $\eta = 0$ at equilibrium. The equilibrium potential E_{eq} is defined by the Nernst equation:

$$E_{eq} = E^{0'} + \frac{RT}{nF} \ln \frac{C_O}{C_R}. \quad [23]$$

The choice of formal potential $E^{0'}$ is arbitrary for a symmetric cell with only one electrochemical couple. For convenience, we simply set $E^{0'} = 0$ and note that using the ferricyanide reduction potential of 0.36 V vs. SHE[23] does not affect our calculations.

Electrochemical boundary conditions.—The boundary conditions related to electrochemical phenomena in the two-dimensional model are shown in Figure 3c. The inlet and exit channels are assumed to be insulating. At each electrode-membrane interface, the electron current i_E is set to zero, and at each electrode-land interface, the ion current i_L is set to zero. One of the lands is grounded ($\phi_E = 0$) while the other is set to a fixed voltage ($\phi_E = V_{app}$) for potentiostatic modeling or a fixed current density ($i_E = i_{in} = i_{app}(W_C + W_L)/W_L$) is imposed. The left and right edges of the model, above the channel center lines, are mirror planes.

Pore-scale mass transport in a homogeneous model.—The surface concentration C_S of an electroactive species in a porous electrode can be modeled through a mass transfer coefficient, k_m. This coefficient has units of cm/s and can be considered an effective diffusivity divided by an effective diffusion boundary layer thickness. Wilson and Geankoplis[24] measured the mass transfer coefficient of a

Table III. Summary of model parameters, values used for those parameters, and sources for those values.

Name	Symbol	Value	Source
Permeability (in-plane)	K_{IP}	1.4×10^{-11} m^2	Measurement
Permeability (through-plane)	K_{TP}	6.6×10^{-12} m^2	Measurement
Viscosity	μ	1.2 mPa s	Measurement
Electrolyte conductivity	κ	0.15 S/cm	Measurement
Specific surface area	a	40 cm^{-1}	Fitted
Electrochemical rate constant	k_0	0.1 cm/s	Fitted
Electronic conductivity	σ_{eff}	6.8 S/cm	20
Mass transfer coefficient	k_m	$\frac{0.832D^{2/3}v_e^{1/3}}{\epsilon d_p^{2/3}}$	4
Ferrocyanide diffusivity	$D_{Fe^{II}}$	7.3×10^{-6} cm^2/s	32
Ferricyanide diffusivity	$D_{Fe^{III}}$	9.0×10^{-6} cm^2/s	32
Porosity	ϵ	0.9	33
Fiber diameter	d_p	10 μm	34
Membrane resistance	r_{mem}	0.625 Ω cm^2	Measurement
Electrode thickness	L_E	200 μm	Gasket thickness

packed bed of benzoic acid spheres under a range of Schmidt[b] and Reynolds numbers to find an empirical correlation; their correlation was amended by Darling and Perry[4] for cylindrical fibers and is given as:

$$k_m = \frac{0.832D^{2/3}|v|^{1/3}}{\epsilon d_p^{2/3}}. \quad [24]$$

In Equation 24, D is the diffusivity of the reacting species (taken to be an average of the ferrocyanide and ferricyanide diffusivities in Table III), ϵ is the porosity, $|v|$ is the magnitude of the volume-averaged velocity, and d_p is the fiber or particle diameter. In this definition, we assume a constant diffusivity and thus k_m is not a function of the concentration of ferrocyanide or ferricyanide.

The mass transfer coefficient is related to the difference between C_S and the bulk concentration in the center of the pore, C_B, by:

$$N_S = k_m(C_B - C_S), \quad [25]$$

where N_S is the flux of electroactive species toward the carbon fiber surfaces within the porous electrode. This flux toward the surface must be balanced by consumption or production of the electroactive species by an electrochemical reaction at the surface of the electrode:

$$Fk_m(C_{R,B} - C_{R,S}) = i_0\left[\frac{C_{R,S}}{C_{R,B}}\exp\left(\frac{\alpha nF}{RT}\eta\right) - \frac{C_{O,S}}{C_{O,B}}\exp\left(\frac{-(1-\alpha)nF}{RT}\eta\right)\right]. \quad [26]$$

In the case of two inter-converting electrochemical reactants O and R, the flux of R toward the surface of the fiber must equal the flux of O away from the fiber. Assuming O and R have equal diffusivities, the surface and bulk concentrations of each species are related by the following equation:

$$C_{R,B} - C_{R,S} = -\left(C_{O,B} - C_{O,S}\right). \quad [27]$$

Equation 24 can be used to calculate k_m in Equation 26. Equations 26 and 27 can then be solved for the surface concentrations $C_{R,S}$ and $C_{O,S}$.

Specific surface area and electrochemical rate constant.—Modeled polarization curves were fitted to experimentally obtained results (see Figures 7 and 9 for experimental results and model best fit). This fitting procedure suggests a specific surface area of 35–45 cm^{-1} and an electrochemical rate constant ranging from 0.05–0.2 cm/s. This range agrees well with reported k_0 values for the ferrocyanide/ferricyanide couple in the literature.[25–27] Note that a and k_0 should be fit independently. At low current density, the overpotential is dominated by kinetic losses which scale as ak_0, but at high current density, a mass transfer limit sets in which scales as ak_m. Additionally, the fitted value for a is much lower than the theoretical value of 400 cm^{-1}, assuming cylinders of diameter 10 μm packed to a porosity of 0.9. This discrepancy suggests that not all the physical surface area of the electrode is electrochemically active, possibly due to incomplete wetting or channeling effects in the electrode, and highlights the need for additional careful study of fluid flow in porous electrodes.

Details of the fitting procedure are listed in the Supplemental Information.

Energy efficiency and effective voltage efficiency.—The energy efficiency, EE, of a flow battery is equal to the product of the current efficiency, CE, and the voltage efficiency on charge, VE_{charge}, and on discharge, $VE_{discharge}$:

$$EE = (CE)(VE_{charge})(VE_{discharge}). \quad [28]$$

In most batteries, the current efficiency is very high (>95%). Furthermore, the current efficiency is usually dominated by reactant crossover, side reactions, or some mixture of the two. We assume these mechanisms are not strongly dependent on flow field configuration. Thus, this work will focus on the effect of flow field design on the voltage efficiency of the cell.

Given a membrane area-specific resistance, r_{mem}, and the electrode overpotentials, η_{pos} and η_{neg}, at a current density, i, the one-way voltage efficiency, VE_{1-way}, can be computed using the following equation:

$$VE_{1-way} = \frac{V_{OC} - ir_{mem} - \eta_{pos} - \eta_{neg}}{V_{OC}} = 1 - \frac{ir_{mem}}{V_{OC}} - \frac{2\eta_{elec}}{V_{OC}} \quad [29]$$

We assume an open circuit voltage V_{OC} of 1.21 V, as seen in cells using the 2,6-dihydroxyanthraquinone (2,6-DHAQ) chemistry paired with the ferrocyanide electrode.[28] Additionally, it is assumed that η_{pos} and η_{neg} are equal and restated as $2\eta_{elec}$. For systems with fast redox kinetics, like 2,6-DHAQ and ferrocyanide, this approximation is reasonable. The electrode overpotential can be calculated from the solid phase potential at the current collector, $\phi_{E,CC}$, and the liquid phase potential at the membrane, $\phi_{L,mem}$:

$$\eta_{elec} = \phi_{E,CC} - \phi_{L,mem} - E_{eq}. \quad [30]$$

The power per unit area consumed by pumping electrolyte at a given area-specific flow rate $\dot{Q}_A$ can be estimated as $\dot{Q}_A\Delta P$, where ΔP is the pressure drop through the cell, as calculated by the three-dimensional fluid dynamic model. Implicit in this estimation of pumping power loss is an unrealistic pumping efficiency of 100%.

[b]The Schmidt number Sc compares the relative effects of momentum transport due to viscous dissipation and species transport due to diffusion, and is the ratio of the kinematic viscosity ν to the diffusivity D: $Sc = \nu/D$.

Therefore, we define a scaling factor S by which we multiply the power lost from pumping, to account for pump inefficiency as follows:

$$S = \frac{1}{\Psi_{pump}} \frac{\mu'}{\mu}. \quad [31]$$

This scaling factor S is the inverse of the pump efficiency Ψ_{pump} for a given viscosity, but can also be used to account for changes in viscosity. In this definition, μ' is the new viscosity value, and μ is the value of 1.2 mPa s measured in this work for an aqueous ferrocyanide-based electrolyte. We set $S = 1.67$, unless noted otherwise, to account for a Ψ_{pump} of 60%, a representative average among several pump types and system configurations.[29] The implications of varying S to account for the change in pumping power losses with increased channel length and fluid viscosity are discussed later. The area-specific pumping power loss, divided by the operating current density i, gives an effective voltage loss due to pumping, used to define a pumping-corrected voltage efficiency VE_{pump}:

$$VE_{pump} = 1 - \frac{i r_{mem}}{V_{OC}} - \frac{2\eta_{elec}}{V_{OC}} - S\frac{\dot{Q}_A \Delta P}{i V_{OC}}. \quad [32]$$

Generating contour maps of flow field efficiencies.—The electrochemical performance and pressure drop of many interdigitated flow field designs was simulated at several current densities and flow rates to evaluate the variation of VE_{pump} with flow field dimensions. The two-dimensional, coupled electrochemical and fluid dynamic model was used to compute η_{elec}, and the three-dimensional fluid dynamic model was used to compute ΔP for values of i ranging from 0.025 to 0.250 A/cm^2 in increments of 0.025 A/cm^2 and values of $\dot{Q}_A$ ranging from 5 to 60 mL min^{-1} cm^{-2} in increments of 5 mL min^{-1} cm^{-2}. The channel and land widths were each varied systematically; simulations were performed with land and channel dimensions of 0.1 mm, and 0.2 to 1.6 mm in 0.2 mm increments. The channel and land widths used are also indicated in Figure 6.

Summary of parameters.—Key parameters for describing the electrochemical behavior of the single-reservoir symmetric ferro-ferricyanide cell are given in Table III.

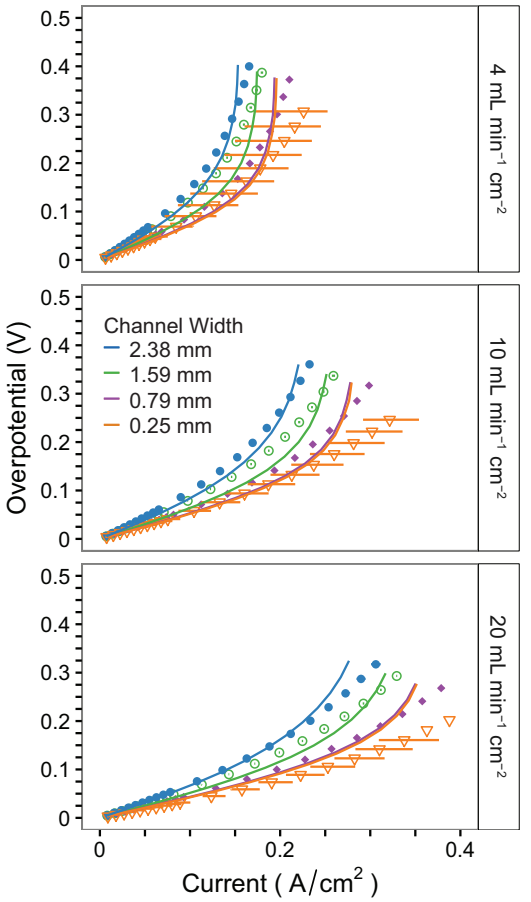

Figure 7. Measured (points) and calculated (lines) polarization curves for four flow fields with varying channel widths at constant land widths. Note that the 0.25 mm wide channels are only 0.25 mm deep, due to machining limitations. The other flow fields have 1.90 mm deep channels. All flow fields shown here have 0.79 mm wide lands.

Results and Discussion

Validating the model with experimental variations of channel and land width in a flow cell.—The effect of varying flow field channel width is shown in Figure 7. As seen in the figure, flow fields with wide channels exhibit greater overpotential losses than flow fields with thin channels. Although the computational model exhibits the correct ranking of flow field designs, it does not fully capture the possible performance improvement associated with very narrow channels. Experimental observations of the 0.25 mm channel flow field also exhibited a wider range of measured current at a given voltage as shown by the larger error bars in those measurements. The experimental error could be due to bubbles or other flow nonidealities associated with extremely narrow channels. For example, a small bubble lodged in a channel could cause the fluid to completely bypass that channel, making the flow field as a whole behave as if it had wider lands. Additionally, as the channel width approaches the electrode pore diameter (about 0.1 mm), the distinction between Navier-Stokes flow in the channel and Darcy flow in the porous medium becomes less clear, and more sophisticated fluid dynamic modeling may be required to accurately predict performance with such narrow channels.

For all flow fields, the measured overpotential is reduced as flow rate is increased. We attribute this reduction in overpotential to enhanced mass transport within the porous electrode. As shown in Equation 24, an increase in the superficial velocity v results in an increase in the mass transfer coefficient k_m. The increase in k_m results in an increase in pore surface concentration C_S for a given value of the flux N_S to the pore surface. Because C_S increases at constant N_S, the overpotential decreases.

The measured and computed pressure drops as functions of flow rate for each channel width are shown in Figure 8. Pressure drop does not monotonically decrease as channel width is increased. As the channels become wider, fewer channels fit within the 5 cm^2 active area, requiring each channel, and the porous medium between each set of channels, to carry more fluid.

The "micro-channel" flow field was constructed with 0.25 mm deep channels rather than 1.90 mm deep channels due to machining limitations. Channel depth is not expected to significantly impact polarization behavior, but the pressure drop from traveling down the channel is likely to increase with shallower channels. To test the relative importance of this effect, the pressure drop through the "micro-channel" flow field was modeled at three different channel depths (Figure 8b). These calculations suggest that deeper channels could alleviate the pressure problem associated with narrow channels, at the possible expense of thicker bipolar plates and channel fabrication costs. At constant area-specific flow rate, there is no pressure penalty to increasing channel depth. Nevertheless, increasing channel depth has diminishing returns on decreasing pressure drop, as the 1.9 mm deep channel exhibits less than a factor of 2 decrease relative to the 0.75 mm deep channel. These diminishing returns can be attributed to the limiting behavior of the hydraulic diameter d_h as H_C increases: d_h approaches $2W_C$ and the pressure drop down the length of the channel becomes dominated by channel width. A true optimization of channel depth would take into account these diminishing returns, the cost of

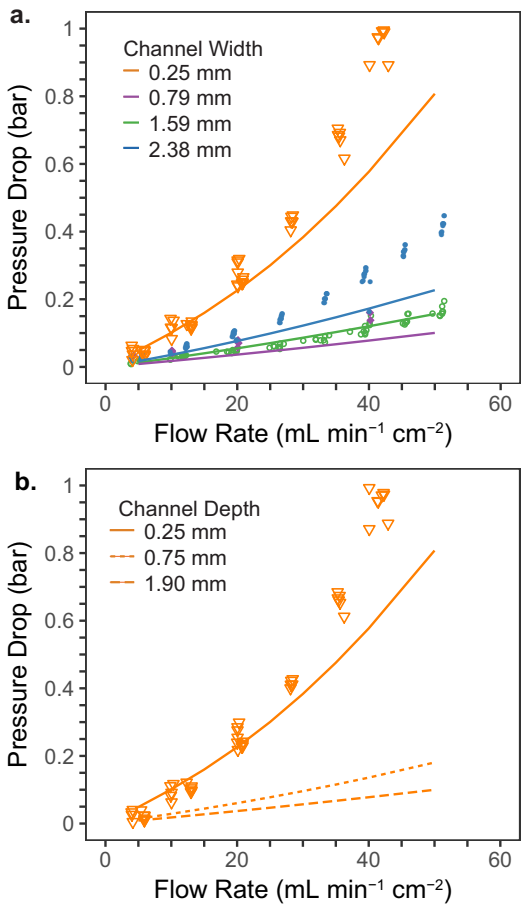

Figure 8. a) Measured (points) and calculated (lines) pressure drop versus flow rate for various channel widths with 0.79 mm wide lands. Note that, due to machining constraints, the 0.25 mm wide channels are only 0.25 mm deep; other channels are 1.90 mm deep. b) Predicted effect of changing channel depth on the pressure drop in the "micro-channel" flow field. Data are for a 0.25 mm wide by 0.25 mm deep channel; all simulations are for 0.25 mm wide channels with depth as indicated.

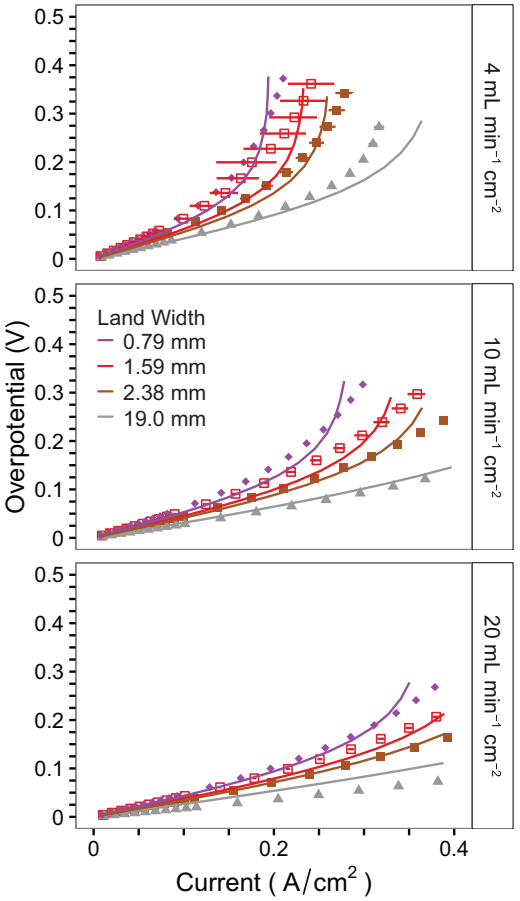

Figure 9. Measured (points) and calculated (lines) polarization curves for three flow fields with varying land widths at constant channel widths. Also included is the flow through flow field that represents the elimination of stagnant zones within the porous electrode to the greatest extent possible in this experiment. Note that the flow-through flow field has 1.59 mm channels while the other flow fields have 0.79 mm wide channels in both simulation and experiment.

thicker bipolar plates, and the potential costs associated with precise manufacturing of deep channels.

The effect on cell performance of varying land width at constant channel width is shown in Figure 9. The widest land width (the "flow-through" flow field) demonstrates the lowest polarization resistance of all flow fields tested. This flow field also has the highest measured pressure drop (Figure 10). Understanding the trade-off between pumping power losses and electrochemical performance gains is discussed later.

In many cases, the electrochemical model tends to underpredict overpotential losses at low current density, and overpredict overpotential losses at high current density. This effect is most evident in the sharp upward curvature of the modeled polarization curves in Figures 7 and 9 relative to experimental measurements at high current density. This difference between model and experiment implies that the observed mass transport effects are more complicated than the simple relationship assumed in Equation 24. The assumed relationship may be relevant for a single pore size; however, a real porous electrode has a distribution of pore sizes, which perhaps leads to the measured overpotential representing the average over locally varying values for a given current density. Additionally, recent experiments[35] have demonstrated different scaling of the mass transfer coefficient with

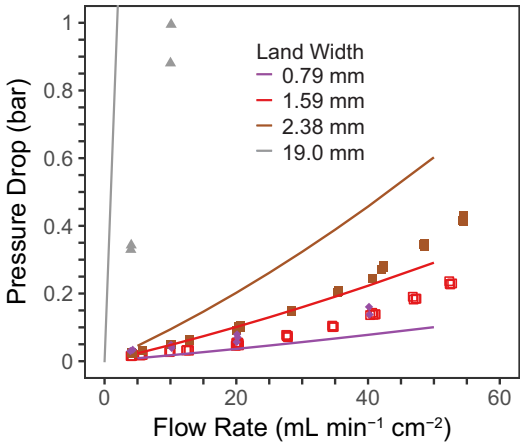

Figure 10. Measured (points) and calculated (lines) pressure drop versus flow rate at various land widths. The predicted pressure drop at 20 mL/min for the "flow-through" flow field is 2.1 bar, and at 50 mL/min it is 6.8 bar. The discrepancy between predicted and measured pressure drop in the "flow-through" flow field could be indicative of flow channeling in the electrode, or flow between the electrode edges and the gasket.

average velocity than the relationship used in this work, which uses local velocity. These deviations highlight the importance of deeper understanding of mass transport in porous electrodes and illustrate a fertile area of further study.

As seen in Figure 10, the model tends to overpredict changes in pressure drop with increasing land width relative to experimental measurements. The model assumes uniform compression of the porous electrode due to its assumption of a constant permeability, whereas an actual porous electrode can relax and expand over the channels where it is unsupported. Additionally, the model assumes all flow through the porous electrode is perpendicular to the channel and neglects the possibility for fluid to flow over the wall at the tips of the inlet channels. This additional fluid pathway could account for some of the reduction in observed pressure, but is likely to become less significant in large-area flow fields, in which the channels are much longer.

Stagnant zones in the electrode.—The observed difference in polarization performance with different flow fields may be due to the existence of stagnant zones within the porous electrode. In an interdigitated flow field, fluid must fill the inlet channel and flow into the electrode, across the land, and out through the exit channel. This flow pattern results in areas of low flow rate above the center lines of the inlet and exit channels. These areas of low flow rate become more easily depleted of reactant and are less well utilized, as seen in Figure 11. These stagnant zones occur close to the membrane, which is also where the highest rate of electrochemical reaction is expected based on the relative values of σ_{eff} and κ_{eff}.[20,30] Thus, ionic current from the membrane must traverse the stagnant zone before converting to electronic current via a faradaic reaction. Because the electrolyte is much less conductive than the electrode, the lengthening of the ionic conduction path results in an increase in Ohmic losses. Therefore, a flow field that contains wider channels, or more total channel area, would show higher overpotential than a flow field with less channel area, or wider lands. A prudent flow field design would make the channels as small as possible, and the lands as wide as possible, without making the cell pressure too high for reasonable operation.

One method to reduce pressure drop is to use a thicker electrode, or stack multiple electrode sheets. Preliminary experiments (see Figure S1, Supplemental Information) demonstrated that stacking multiple electrodes increased overpotential losses, so we chose to focus our studies on a single electrode sheet of approximately 200 μm compressed thickness. These small overpotential penalties could be mitigated by increasing land width, as the increase in pumping power loss with increasing land width would be less for a thicker electrode. It is unclear whether the overall performance benefit would justify the financial cost of using additional electrode material.

The effect of varying channel and land width.—The modeling and experimental results in this work suggest two main strategies:

- To minimize overpotential losses, the lands must be wide and the channels narrow, and
- To minimize pumping power losses, the lands must be narrow, and the channel width appropriately optimized.

The effects of electrochemical and pumping power losses can be offset by incorporating them into a single pumping-corrected voltage efficiency, VE_{pump} (Equation 32). Results from a pumping-corrected voltage efficiency calculation with an operating current density of 0.25 A/cm^2 and a flow rate of 20 mL min^{-1} cm^{-2} are shown in Figure 12. Under these conditions, the maximum VE_{pump} was calculated for a 0.4 mm channel width and a 0.6 mm land width. The model also indicates that the "Equal" flow field ($W_C = 0.79$ mm, $W_L = 0.79$ mm) has a VE_{pump} within 1% of the maximum.

The results in Figure 12a suggest the existence of a finite channel width that minimizes pressure drop for a given land width and area-specific flow rate. This channel width is not necessarily an optimum for all systems, however. Simulation of larger systems, as discussed in the section on the effects of additional pumping power losses, reveals that the optimal channel width changes as a function of channel length.

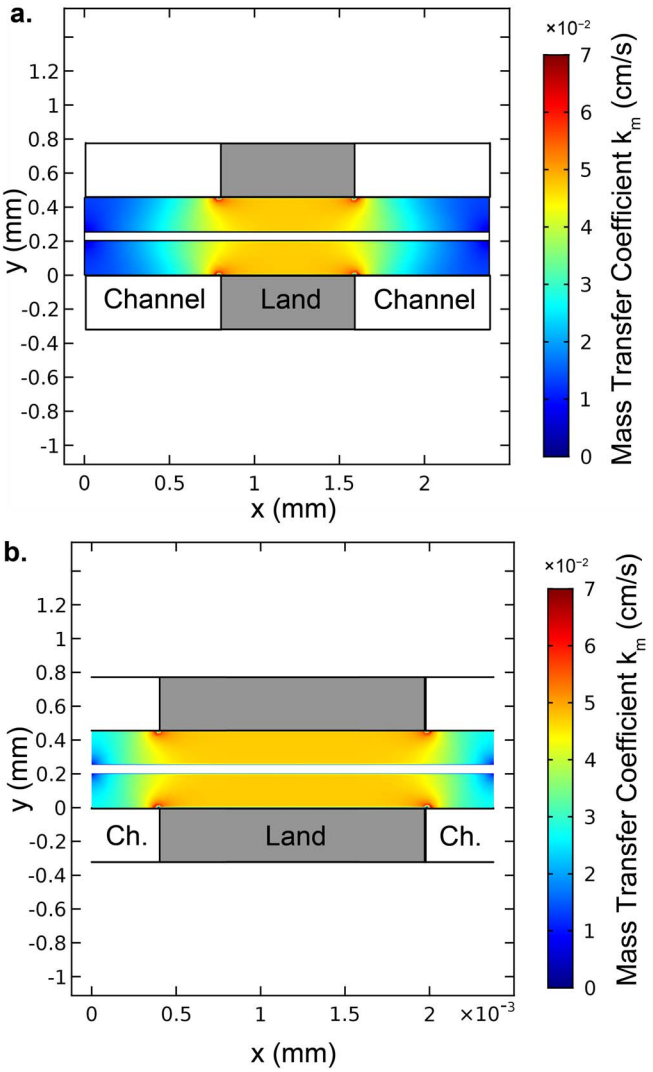

Figure 11. Color map of the mass transfer coefficient in a) the "wide channel" flow plate (1.59 mm channels, 0.79 mm lands) and b) the "wide land" flow plate (0.79 mm channels, 1.59 mm lands). The mass transfer coefficient is significantly reduced above the center line of the channel near the membrane, because the superficial velocity there is lowest, resulting in a stagnant zone. Flow fields with larger channels relative to lands should therefore demonstrate higher overpotential at a given current.

To explore the generality of the optimum in Figure 12 as a function of flow rate, the model was run at a range of flow rates from 5 mL min^{-1} cm^{-2} to 50 mL min^{-1} cm^{-2} in 5 mL min^{-1} cm^{-2} increments. It was then assumed that the flow rate is an easily adjustable parameter in an operating flow battery; that is, at a given current density, a flow battery operator could choose to increase or decrease pumping rate to maximize VE_{pump}. Under this assumption, the flow rate results can be combined into a single graph, as shown in Figure 13, in which each flow field is assumed to be operating at its most efficient flow rate for the specified current density of 0.250 A/cm^2. These results demonstrate that the optimum channel width does not change, but a wider range of land widths becomes accessible because the flow rate can be increased or decreased to accommodate narrow or wide lands respectively. Throughout the remainder of this work, this optimization process with respect to flow rate will be

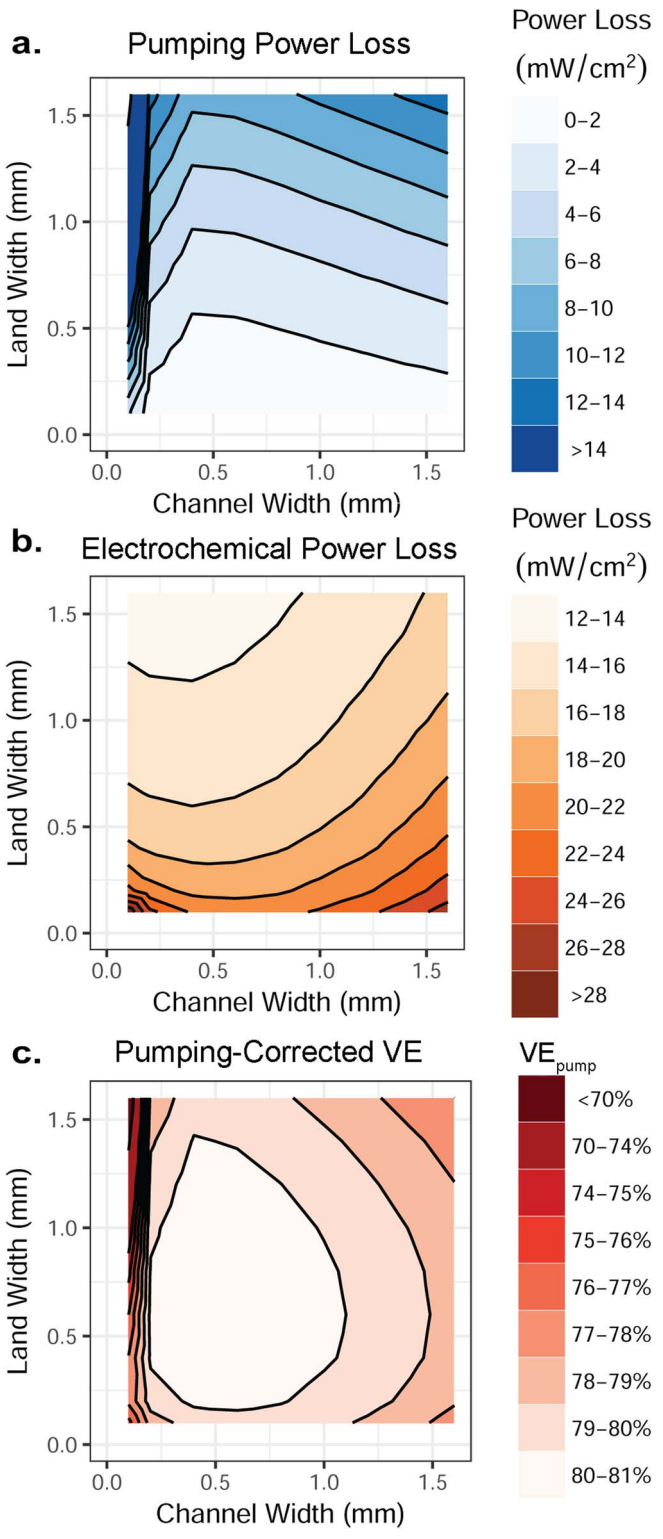

Figure 12. Example calculations of (a) pumping and (b) electrochemical power losses in a ferrocyanide/ferricyanide porous electrode. The flow rate is 100 mL/min and the applied current density 0.25 A/cm^2. c) Pumping-corrected voltage efficiency as calculated from Equation 29, assuming a V_{OC} of 1.21 V, a S of 1.67, a current of 0.25 A/cm^2, and a flow rate of 20 mL min^{-1} cm^{-2}. There is an optimum pumping-corrected voltage efficiency at approximately 0.4 mm channel width and 0.6 mm land width. Contours are drawn based on linear interpolation between the simulation points shown in Figure 6.

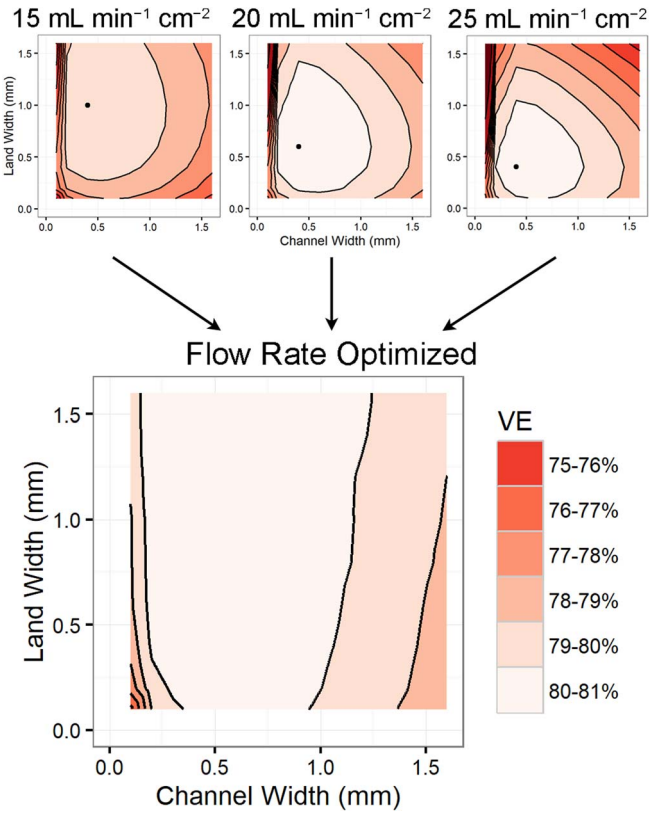

Figure 13. An illustration of the process of optimizing over flow rate. The results from computations at various flow rates are combined to produce a single map of VE_{pump} optimized with respect to flow rate. The operating current density was 0.25 A/cm^2.

used to illustrate the range of high-efficiency land and channel widths available.

Model sensitivity to fitting parameters.—The specific surface area, a, and electrochemical rate constant, k_0, were used as fitting parameters on a set of experimental data. To evaluate the model sensitivity to these parameters, the effect of independently varying a and k_0 was explored for a variety of channel and land widths. Pumping-corrected voltage efficiency at 0.125 A/cm^2 for a variety of specific surface area values is shown in Figure 14. The specific surface area shows diminishing gains in energy efficiency as it is increased from 20 cm^{-1} to 400 cm^{-1}. Furthermore, changing the specific surface area does not appear to have a strong effect on the optimal interdigitated flow field design. The electrochemical rate constant has a similarly weak effect on the optimal flow field and efficiency (Figure 15).

The effect of varying operating current.—Changes in the operating current can also significantly impact VE_{pump}. According to Equation 32, VE_{pump} losses from Ohmic conduction in the membrane (ir_{mem}/V_{OC}) scale linearly with current, whereas pumping power losses ($SQ_A\Delta P/iV_{OC}$) scale inversely with current. The electrode overpotential, η_{elec}, is a combination of linear Ohmic effects from electrode and electrolyte conduction and nonlinear electrochemical kinetic and mass transport effects and generally increases as current density increases.

As shown in Figure 16, large gains in VE_{pump} are obtained from significantly decreasing operating current density. Most of these gains can be attributed to decreasing the voltage loss due to membrane resistance. The voltage efficiency loss from Ohmic conduction through the membrane (ir_{mem}/V_{OC}) is given in Table IV for reference and

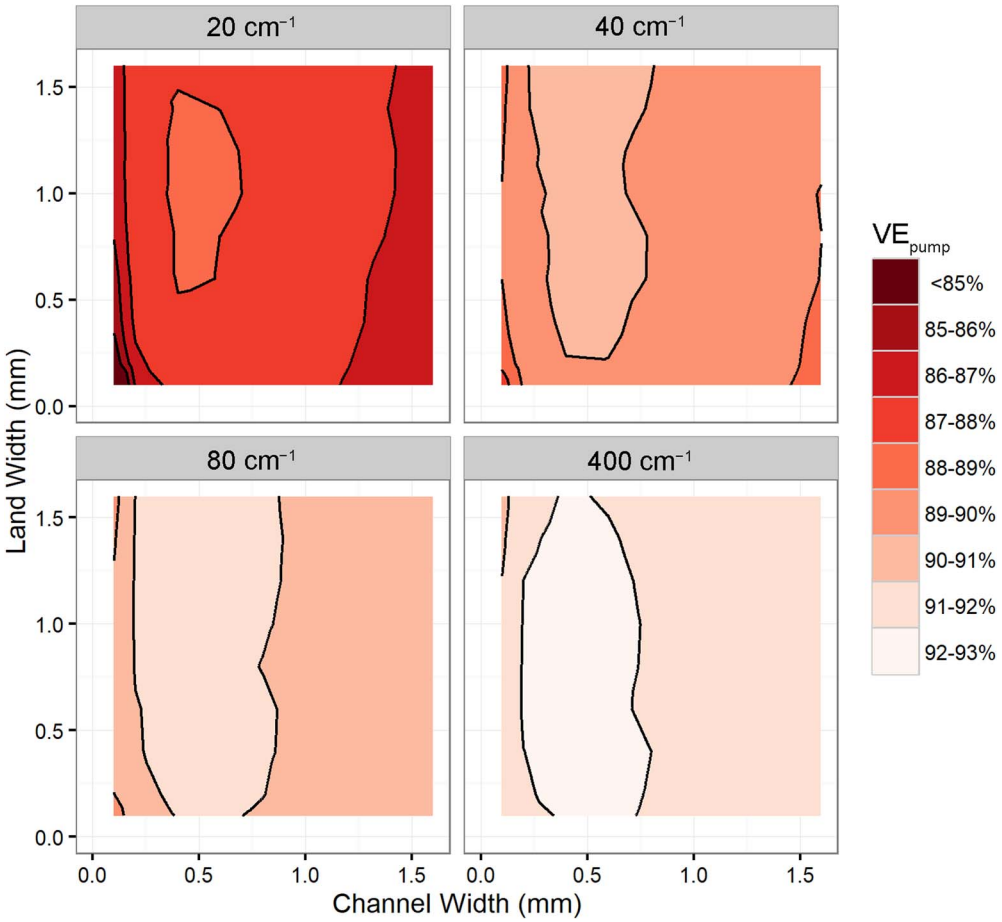

Figure 14. Pumping-corrected voltage efficiency at optimal flow rate for several values of the specific surface area a. The applied current density was 0.125 A/cm^2. At this current density, 6.5% efficiency loss is attributed to resistive losses in the membrane.

to permit adaptation of the model results to systems with different Ohmic losses. Furthermore, the range of high-efficiency flow fields varies only slightly with current density: the most efficient flow fields at 0.125 A/cm^2, with land widths between 0.5 and 1.0 mm and channel widths between 0.4 and 0.8 mm, are also the most efficient flow fields at other current densities. This result indicates that a single flow field can be built and used at a variety of operating currents. This result further demonstrates the generality of the optimal flow field discussed above.

The effect of varying state of charge.—Ideally, the highest efficiency flow fields would maintain high-efficiency operation throughout a charge-discharge cycle. Variations in state of charge, and therefore an entire charge-discharge cycle, can be modeled by changing the inlet concentration ratio of ferrocyanide to ferricyanide. The state of charge is defined as the ratio of ferricyanide ion to total ferrocyanide and ferricyanide concentration:

$$SOC = \frac{C_{Fe^{III}}}{C_{Fe^{II}} + C_{Fe^{III}}}. \quad [33]$$

The effect of varying state of charge is shown in Figure 17 for 0.125 A/cm^2 applied current. As shown, the prediction of the model for the most efficient flow field hardly varies with state of charge. The maximum VE_{pump}, however, does decrease at extreme states of charge.

The area-specific power loss from pumping ($\dot{Q}_A \Delta P$) and from electrode overpotentials ($2i\eta_{elec}$) are shown in Figure 18. This combined area-specific power loss, p_{loss}, combined with a known area-specific membrane resistance, r_{mem}, enables calculation of the maximum deliverable power, p_{max}, at each state of charge:

$$p_{max} = iV_{OC} - i^2 r_{mem} - p_{loss}, \quad [34]$$

in which V_{OC} is the open circuit voltage at the given state of charge.

In both Figure 17 and Figure 18, an interesting symmetry is present: the VE_{pump} map on discharging at 90% SOC is similar to the VE_{pump} map on charging at 10% SOC, and the results for discharging at 10% SOC are similar to the results for charging at 90% SOC. The power loss results for each pair are exactly the same. This symmetry in power loss arises from the assumed reversibility of the ferrocyanide-ferricyanide redox couple: the kinetic overpotential for a 10% SOC electrolyte during discharge is equivalent to that of a 90% SOC electrolyte during charge. Furthermore, the fluid viscosity and mass transfer coefficient are assumed not to be functions of state of charge, so the pumping

Table IV. Voltage efficiency loss from Ohmic conduction through the membrane at various applied current densities.

i_{app} A/cm^2	ir_{mem}/V_{OC} –
0.025	0.013
0.125	0.065
0.200	0.103
0.250	0.129

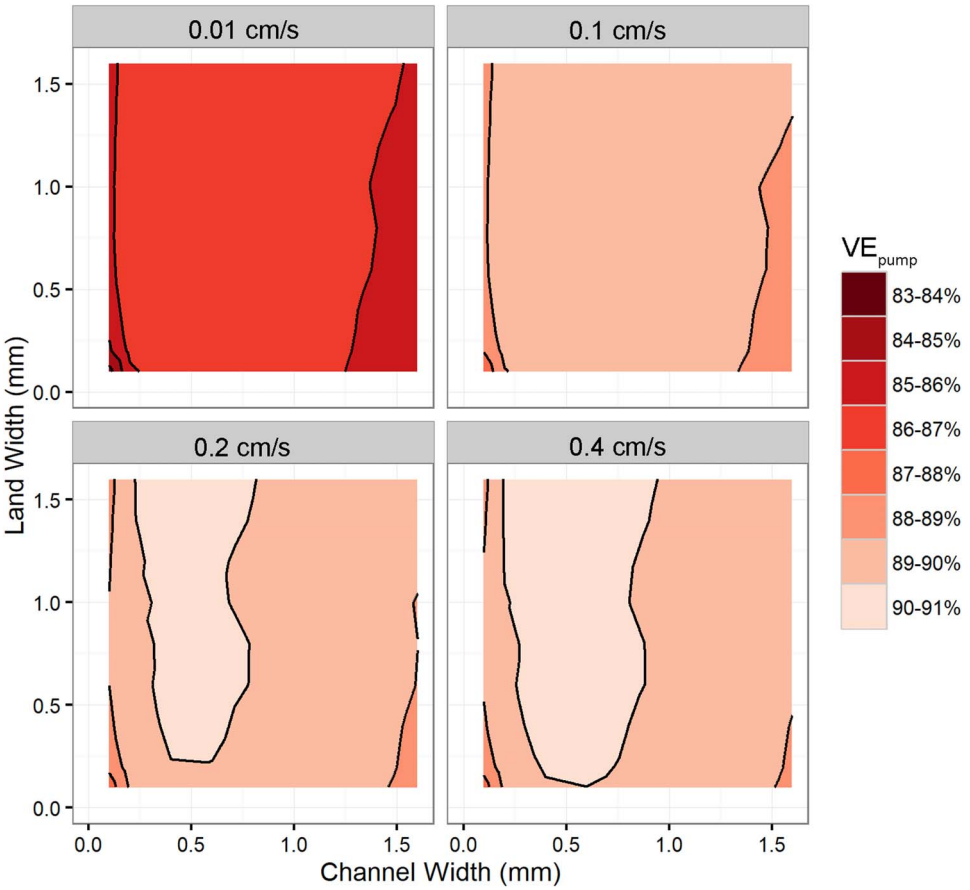

Figure 15. Pumping-corrected voltage efficiency at optimal flow rate for several values of the electrochemical kinetic rate constant k_0. The applied current density was 0.125 A/cm^2. At this current density, 6.5% efficiency loss is attributed to resistive losses in the membrane.

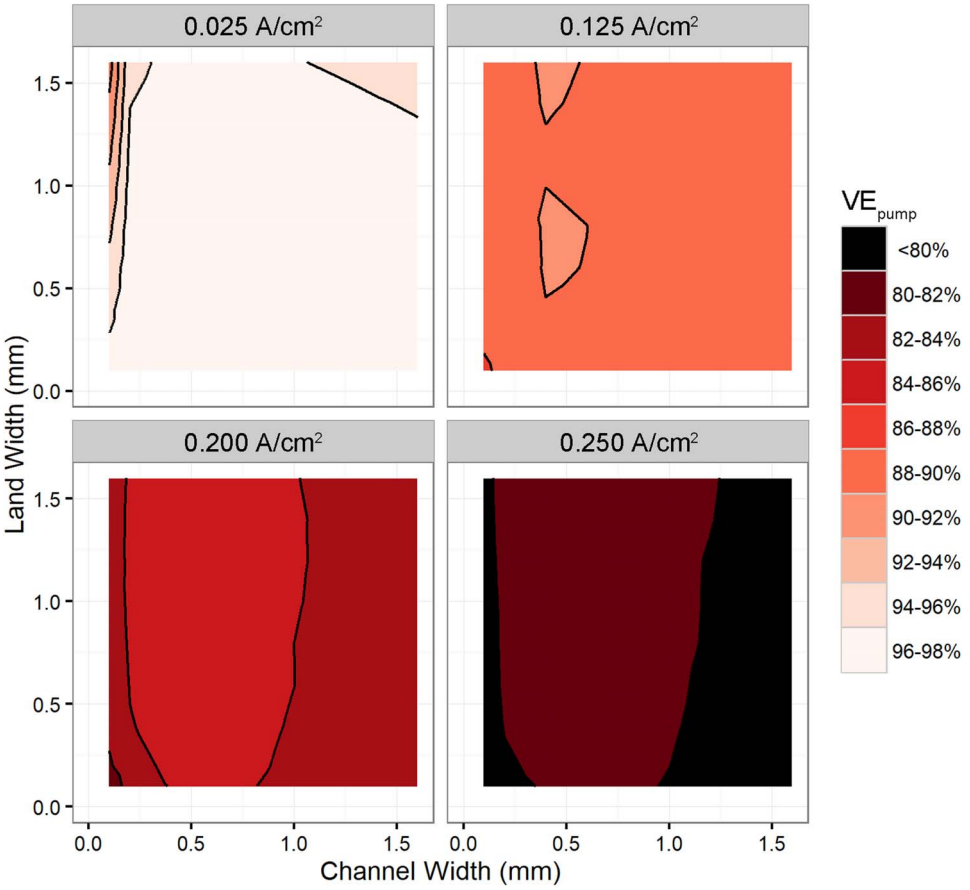

Figure 16. Simulated VE_{pump} at various applied current densities. Much of the efficiency loss is dominated by resistive losses in the membrane, as evidenced by the high voltage efficiencies at low current density. The resistive losses as a percentage of voltage efficiency are listed in Table IV.

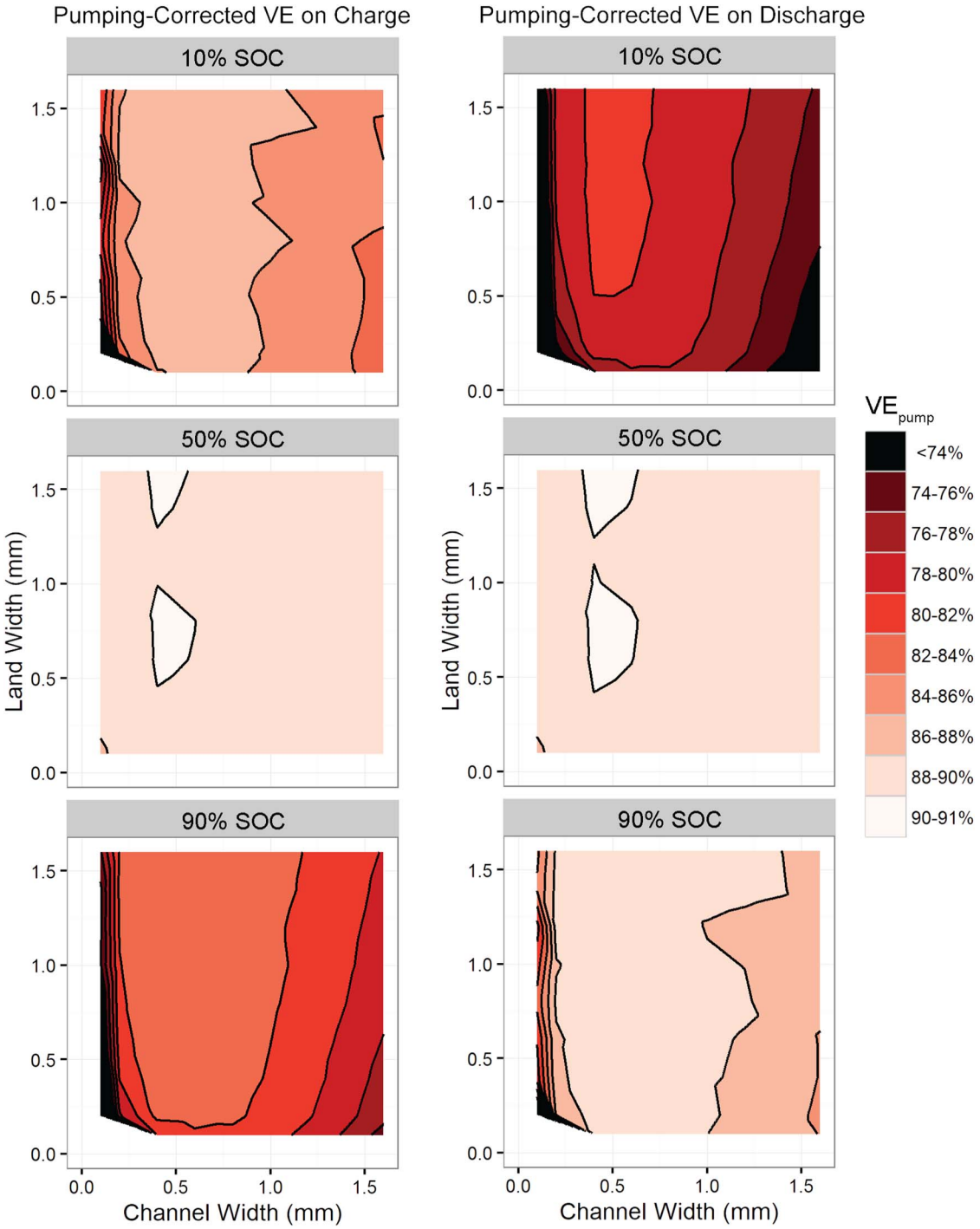

Figure 17. Effect of state of charge on pumping-corrected voltage efficiency during charging and discharging for various channel and land widths. The applied current was 0.125 A/cm^2. At this current density, 6.5% voltage efficiency is lost due to resistance of the membrane. In general, the optimal flow field is not a strong function of state of charge, but the efficiency does change significantly.

power losses and mass transfer overpotentials are equivalent for each pair of results. The major difference from 10% to 90% SOC is the change of the open-circuit potential due to the concentration changes as described by the Equation 23. The difference in V_{OC} between 10% and 90% SOC results in different values of VE_{pump} in Figure 17 despite the identical power losses shown in Figure 18.

The effects of additional pumping power losses.—Power losses due to pumping the electrolyte are not necessarily negligible compared to the inefficiencies resulting from the various overpotentials in the cell. For example, an extremely viscous fluid, inefficient pumps, or a low-permeability electrode would result in greater pumping power losses. To identify cell configurations for which the pumping power losses significantly exceed electrochemical losses, we varied the pumping power scaling factor S through two orders of magnitude as shown in Figure 19. These results demonstrate that a well-chosen land and channel width can produce reasonably high pumping-corrected voltage efficiencies even with extremely inefficient pumps

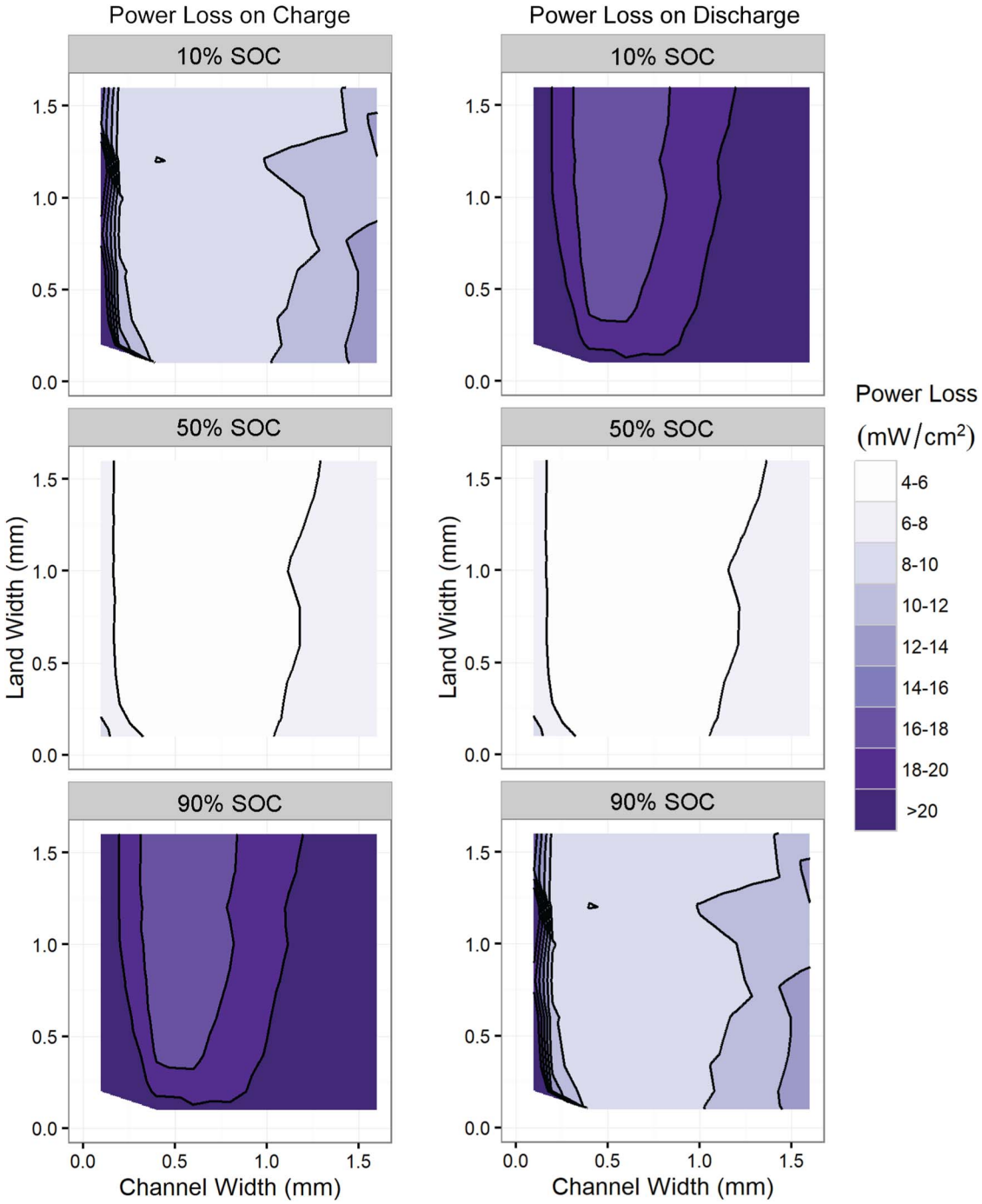

Figure 18. Effect of state of charge variation on power losses, including pumping power losses and electrode overpotential losses, at 0.125 A/cm^2 applied current in both charging and discharging modes. This power loss does not include Ohmic losses of 10 mW/cm^2 from ion conduction through the membrane.

or fluids significantly more viscous than the ferrocyanide/ferricyanide aqueous electrolyte studied here. For example, an increase of S from 1.67 to 10, equivalent to an increase of the electrolyte viscosity from 1.2 mPa s to 7.2 mPa s, results in only a 1% drop in VE_{pump} for most flow fields.

For $S = 100$, pumping power losses become significant and efficient operation is restricted to narrow land widths as shown in Figure 19. Under these conditions, the highest VE_{pump} occurs at the lowest area-specific flow rate studied, 5 mL min^{-1} cm^{-2}, for all flow field dimensions. Furthermore, VE_{pump} is dominated by pumping power losses, as indicated by the similarity in contour shape between Figure 12a and the $S = 100$ panel of Figure 19.

The effect of increasing channel length.—The laboratory-scale systems studied here used a channel length of 2.23 cm, whereas industrial-scale systems have much larger flow fields, with channel lengths on the order of 1 m.[31] Longer channel lengths increase pressure drop, and thereby increase pumping power losses, for constant area-specific flow rate, land width, channel width, and viscosity, as shown in Equations 9 to 11. We use the analytical model from Darling and Perry [4] to compute the pressure drop of longer-channel interdigitated flow fields with either 22.3 cm or 100 cm channel lengths for all values of $\dot{Q}_A$, W_C, and W_L, and match these results with the electrochemical power loss model to compute the flow-rate-optimized value of VE_{pump} for each channel and land width. As shown in Figure 5 and

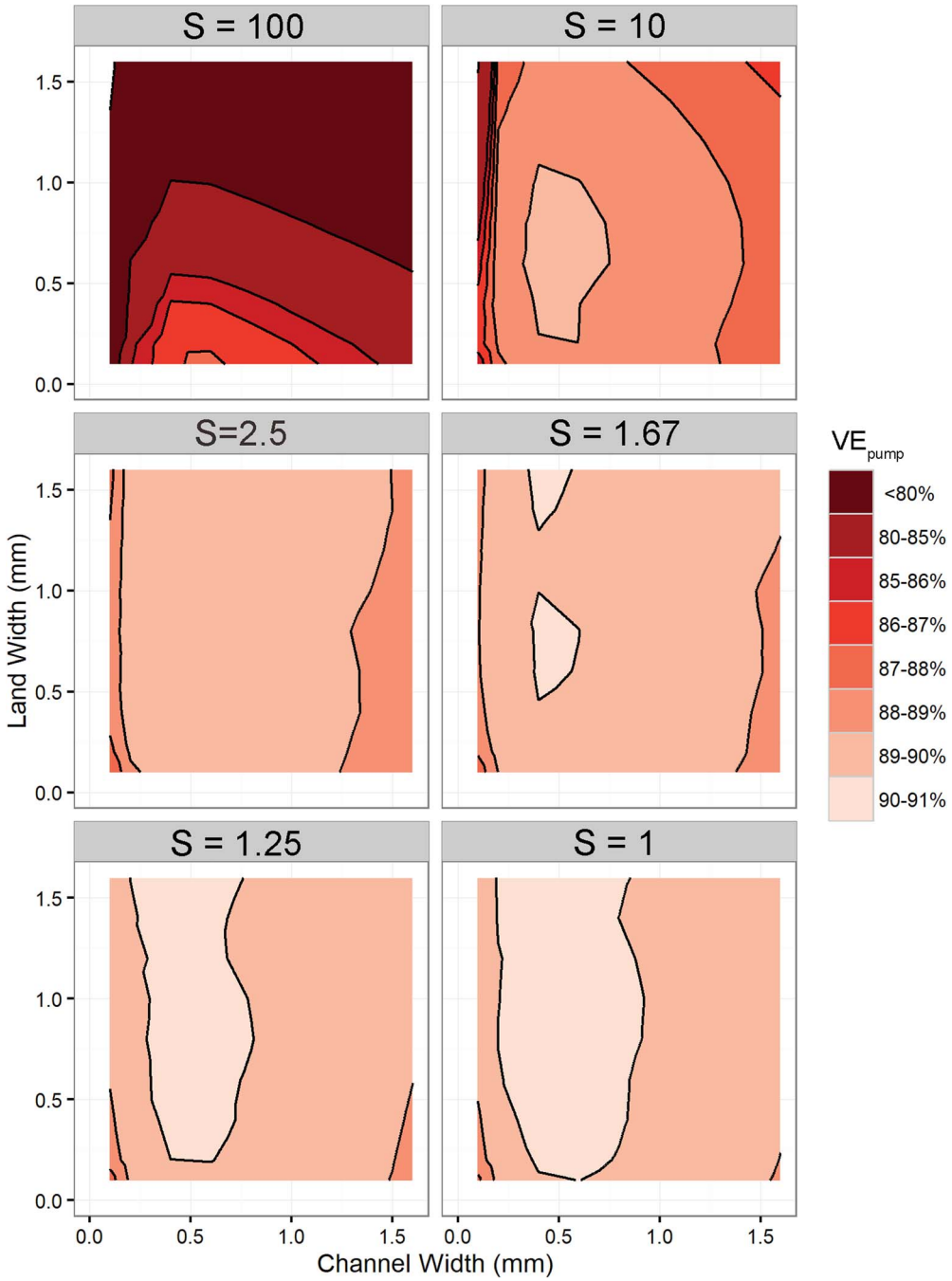

Figure 19. Effect of varying the magnitude of pumping power losses on pumping-corrected voltage efficiency. The parameter S is a dimensionless ratio of viscosity to pump efficiency defined in Equation 31. An S value of 1.67 corresponds to our baseline simulations, using the parameters reported in Table III and $\Psi_{pump} = 60\%$.

discussed earlier, this analytical model predicts similar pressure drop as the three-dimensional model, but requires significantly less computational resources. It must be noted, however, that these efficiencies in computation come at the potential inaccuracy of neglecting the impact of velocity variations on mass transfer effects. Although the analytical model accounts for the possibility of the flow rate changing down the channel, the use of a single two-dimensional flow distribution in the electrochemical model limits the accuracy of our mass transport overpotential calculations.

Maps of VE_{pump} over the explored channel and land width space are shown in Figure 20, along with the pumping power losses, at an operating current density of 0.125 A cm^{-2}. The pumping-corrected voltage efficiency for the 100 cm long channels is dominated by pumping power losses, particularly for very narrow channel widths, because the pressure drop due to fluid flow along the channel is significant. This increased pressure drop results in substantially higher power losses due to pumping for long-channel flow fields, as shown in Figure 20b. For wide channels and narrow lands, reasonably efficient operation is still possible, even for long channels. The maximum VE_{pump} observed in these calculations for a 100 cm long channel is 84.9%, whereas for 2.23 cm long channels it is 90.1%.

The additional pumping power losses resulting from scaling up the channel length can be addressed in several ways. First, the pumping power loss scaling factor S could be decreased, by using a more

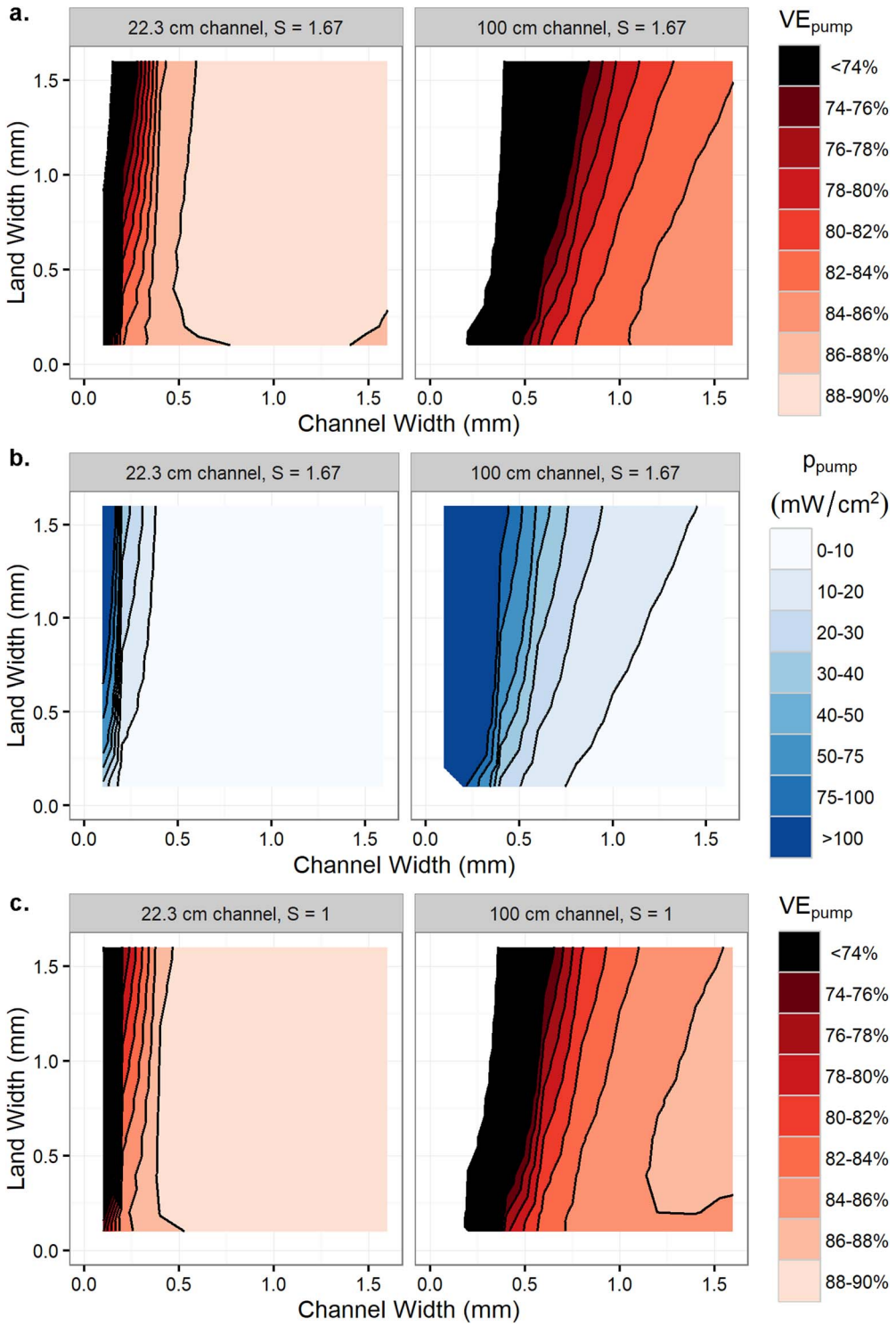

Figure 20. a) Pumping-corrected voltage efficiency maps for interdigitated flow fields with longer channels. The channels were lengthened to 22.3 cm and to 100 cm as listed above each figure. The applied current density was 0.125 A cm^{-2}. The white area in the top left corner of each graph indicates that $VE_{pump} < 0$, which occurs when the pumping power losses are greater than the power delivered; that is, the pumps require more energy to operate than the flow battery can output. With a channel length of 22.3 cm, reasonably high values of VE_{pump} can still be achieved with sufficiently wide channels. At 100 cm channel length, VE_{pump} decreases substantially for channel widths narrower than 0.5 mm. b) Pumping power losses for interdigitated flow fields under the same conditions. For 22.3 cm long channels, the pumping power losses are similar in magnitude to electrochemical power losses (≈10 mW cm^{-2}), but for 100 cm long channels, pumping power losses become much larger in magnitude and dominate the calculation of VE_{pump}. c) Pumping-corrected voltage efficiency maps for the same flow fields, under the same conditions, with the pressure scaling factor S set to 1 instead of 1.67. The pumping-corrected voltage efficiency increases further for the 100 cm long channels.

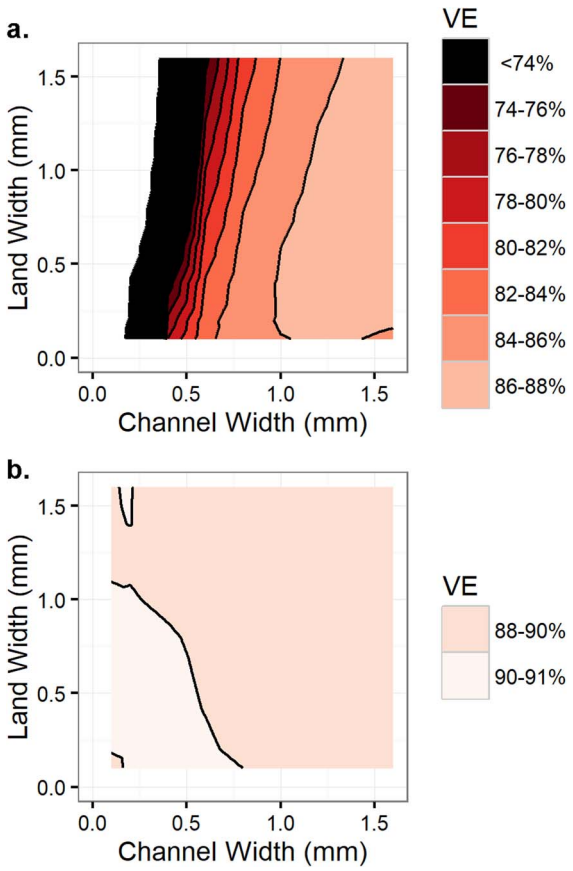

Figure 21. The effects of varying channel depth on pumping-corrected voltage efficiency for a 100 cm long channel at an operating current of 0.125 A cm^{-2}, assuming either a) a channel depth of 3 mm or b) an infinitely deep channel. $S = 1.67$ in both simulations.

efficient pump, a less viscous fluid, or a combination of the two. Reducing S from 1.67 to 1, as shown in Figure 20c, results in an increase in pumping-corrected voltage efficiency, with a maximum VE_{pump} of 86.4% for 100 cm long channels.

Another method to alleviate the issue of large channel pressure drop is simply to make the channels deeper. Figure 21a illustrates the effect of slightly increasing channel depth, from 1.9 mm to 3.0 mm, on VE_{pump}, for a flow field with 100 cm long channels. This increase in channel depth results in an increase in the maximum VE_{pump} to 86.9% (2.0% above the base case of 84.9%), and in general shows similar VE_{pump} values as Figure 20c, in which the pressure scaling factor S was reduced. This result indicates that properly sized channels can be as effective as highly-efficient pumps in improving the pumping-corrected voltage efficiency of a flow battery system.

Figure 21b demonstrates the limiting case of an infinitely deep, 100 cm long channel. Under these conditions, the pressure drop down the channel becomes negligible, and the overall pressure drop is dominated by Darcy flow through the electrode as described by Equation 13. In this idealized case, VE_{pump} values greater than 88% are observed for all channel and land widths studied, indicating that most of the efficiency losses for 100 cm long channels less than about 0.5 mm wide are attributable to the pumping power required to drive fluid down the channel.

Conclusions

In this work, a combined fluid dynamic and electrochemical model was developed to study the dependence of electrochemical and pumping power losses on the channel and land widths of an interdigitated flow field. This model was fit to a set of experimental results from ferrocyanide-ferricyanide symmetric one-reservoir cells with varying channel and land width dimensions. The effect of varying flow fields on electrochemical performance and pressure drop was evaluated experimentally and explained with a computational model. Using the model, the pumping-corrected voltage efficiency was optimized as a function of channel and land width in an interdigitated flow field. The pumping-corrected voltage efficiency surface is rather flat, and flow fields with lands of any width studied here (0.1 mm to 1.6 mm) and channels of a width between 0.4 mm and 0.8 mm are within 1% of the maximum pumping-corrected voltage efficiency for short channel lengths (2.23 cm). This high-efficiency region persists for large variation in operating parameters such as flow rate, current density, and state of charge, as well as engineering parameters such as pumping efficiency, electrode specific surface area, and electrochemical rate constant.

The pumping-corrected voltage efficiency was found to vary substantially when the channel length was increased to industrial scales (1 m). We found that, although large-scale systems will suffer inefficiency due to pumping power losses, these pumping power losses can largely be mitigated by using wider channels, resulting in slightly more than 5% efficiency loss relative to laboratory-scale systems. This efficiency loss can be further reduced to 3% by using deeper channels or more efficient pumps. Overall, these findings illustrate the importance of adequately designing flow fields to reduce stagnant fluid zones and minimize pressure drop.

Acknowledgments

This work was partially funded by ARPA-E Award # DE-AR0000348 and partially funded through the Harvard John A. Paulson School of Engineering and Applied Sciences. This work was also supported by funding from the Massachusetts Clean Energy Technology Center. We acknowledge Marc-Antoni Goulet, Roy Gordon, Alán Aspuru-Guzik, Iryna Zenyuk, Diana De Porcellinis, and Ertan Agar for helpful discussions. We thank Stan Cotreau and the Harvard Physics/SEAS Instructional Machine Shop for assistance with graphite machining.

List of Symbols

a	specific surface area, cm^{-1}
A	area, cm^2
c_F	Forchheimer drag coefficient
C	concentration, mol/L
C_i	concentration of species i, mol/L
$C_{i,in}$	inlet concentration of species i, mol/L
CE	current efficiency
d_h	hydraulic diameter, cm
d_p	fiber diameter, cm
D	diffusion coefficient, $cm^2\ s^{-1}$
D_i	diffusion coefficient of species i, $cm^2\ s^{-1}$
EE	energy efficiency
E_{eq}	equilibrium potential, V
F	Faraday's constant, 96 485 C/mol
H_C	channel height, cm
i	current density, A/cm^2
i_0	exchange current density, A/cm^2
k_0	electrochemical rate constant, cm/s
k_m	mass transfer coefficient, cm/s
K	permeability, m^2
L	length, cm
L_C	channel length, cm
L_E	electrode thickness, μm
n	number of electrons
N	molar flux, mol $cm^{-2}\ s^{-1}$
$N_{C,in}$	number of inlet channels
N_i	molar flux of species i, mol $cm^{-2}\ s^{-1}$

p	power density, W/cm^2
P	pressure, Pa
$P_{\text{in}}^{\text{2D}}$	inlet boundary pressure for 2D model, Pa
$P_{\text{in}}^{\text{3D}}$	inlet boundary pressure for 3D model, Pa
$\dot{Q}$	volumetric flow rate, mL min^{-1}
$\dot{Q}_A$	area-specific flow rate, mL min^{-1} cm^{-2}
$\dot{Q}_T$	total volumetric flow rate, mL min^{-1}
r	radius, cm
r_{mem}	membrane area-specific resistance, Ω cm^2
R	gas law constant, 8.314 J mol^{-1}
R_i	generation rate of species i, mol L^{-1} s^{-1}
S	pumping power scaling factor
T	temperature, K
v	velocity, cm/s
v_S	stream velocity, cm/s
v_V	volume-averaged velocity, cm/s
V	voltage, V
VE	voltage efficiency
VE_{pump}	pumping-corrected voltage efficiency
V_{OC}	open-circuit voltage, V
W_C	channel width, mm
W_{FF}	width of flow field, cm
W_L	land width, mm

Greek

α	charge transfer coefficient
ζ	dimensionless geometric parameter
ϵ	porosity
η	overpotential, V
κ	electrolyte conductivity, S/cm
μ	viscosity, Pa s
ρ	density, g/cm^3
σ	electronic conductivity, S/cm
ϕ	electric potential, V
Ψ_{pump}	pump efficiency

Subscripts

app	applied
B	bulk
CC	current collector
e	exit
eff	effective
E	electrode
in	inlet
IP	in-plane
L	electrolyte (liquid)
mem	membrane
O	oxidized
PFF	parallel flow field
R	reduced
S	surface
TP	through-plane

ORCID

Michael R. Gerhardt https://orcid.org/0000-0002-1272-3607
Andrew A. Wong http://orcid.org/0000-0002-1912-7357
Michael J. Aziz https://orcid.org/0000-0001-9657-9456

References

1. G. L. Soloveichik, *Chem. Rev.*, **115**, 11533 (2015).
2. A. Z. Weber, M. M. Mench, J. P. Meyers, P. N. Ross, J. T. Gostick, and Q. Liu, *J. Appl. Electrochem.*, **41**, 1137 (2011).
3. M. L. Perry, R. M. Darling, and R. Zaffou, *ECS Trans.*, **53**(7), 7 (2013).
4. R. M. Darling and M. L. Perry, *J. Electrochem. Soc.*, **161**(9), A1381 (2014).
5. X. Li and I. Sabir, *Int. J. Hydrogen Energy*, **30**(4), 359 (2005).
6. E. Knudsen, P. Albertus, K. T. Cho, A. Z. Weber, and A. Kojic, *J. Power Sources*, **299**, 617 (2015).
7. J. Marschewski, L. Brenner, N. Ebejer, P. Ruch, B. Michel, and D. Poulikakos, *Energy Environ. Sci.*, **10**, 780 (2017).
8. J. Houser, A. Pezeshki, J. T. Clement, D. Aaron, and M. M. Mench, *J. Power Sources*, **351**, 96 (2017).
9. C. R. Dennison, E. Agar, B. Akuzum, and E. C. Kumbur, *J. Electrochem. Soc.*, **163**(1), A5163 (2015).
10. A. A. Shah, M. J. Watt-Smith, and F. C. Walsh, *Electrochimica Acta*, **53**(27), 8087 (2008).
11. A. A. Shah, R. Tangirala, R. Singh, R. G. A. Wills, and F. C. Walsh, *J. Electrochem. Soc.*, **158**(6), A671 (2011).
12. K. W. Knehr, E. Agar, C. R. Dennison, A. R. Kalidindi, and E. C. Kumbur, *J. Electrochem. Soc.*, **159**(9), A1446 (2012).
13. Z. Wei, J. Zhao, M. Skyllas-Kazacos, and B. Xiong, *J. Power Sources*, **260**, 89 (2014).
14. A. Tang, J. McCann, J. Bao, and M. Skyllas-Kazacos, *J. Power Sources*, **242**, 349 (2013).
15. M. Skyllas-Kazacos, J. McCann, Y. Li, J. Bao, and A. Tang, *ChemistrySelect*, **1**, 2249 (2016).
16. Q. Xu, T. S. Zhao, and P. K. Leung, *Appl. Energy*, **105**, 47 (2013).
17. K. Yaji, S. Yamasaki, S. Tsushima, T. Suzuki, and K. Fujita, *Struct. Multidisc. Optim.*, **57**(2), 535 (2018).
18. K. Oh, T. J. Kang, S. Park, M. C. Tucker, A. Z. Weber, and H. Ju, *Electrochimica Acta*, **230**, 160 (2017).
19. M. D. R. Kok, A. Khalifa, and J. T. Gostick, *J. Electrochem. Soc.*, **163**(7), A1408 (2016).
20. Q. Chen, M. R. Gerhardt, and M. J. Aziz, *J. Electrochem. Soc.*, **164**(6), A1126 (2017).
21. J. P. Feser, A. K. Prasad, and S. G. Advani, *J. Power Sources*, **162**(2), 1226 (2006).
22. D. A. Nield and A. Bejan, *Convection in Porous Media*, Springer Sciece+Business Media, New York (1992).
23. P. Vanysek, in *CRC Handbook Chem. Phys.*, 98th ed., J. R. Rumble, Editor, p. 5–77, Taylor & Francis Group, Boca Raton, FL (2018).
24. E. J. Wilson and C. J. Geankoplis, *Ind. Eng. Chem. Fundam.*, **5**, 9 (1966).
25. I. Hu, D. H. Karweik, and T. Kuwana, *J. Electroanal. Chem.*, **188**, 59 (1985).
26. D.H. Angell and T. Dickinson, *J. Electroanal. Chem.*, **35**, 55 (1972).
27. L.M. Peter, W. Dürr, P. Brinda, and H. Gerischer, *J. Electroanal. Chem.*, **71**, 31 (1976).
28. K. Lin, Q. Chen, M. R. Gerhardt, L. Tong, S. B. Kim, L. Eisenach, A. W. Valle, D. Hardee, R. G. Gordon, M. J. Aziz, and M. P. Marshak, *Science*, **349**(6255), 1529 (2015).
29. V. Viswanathan, A. Crawford, D. Stephenson, S. Kim, W. Wang, B. Li, G. Coffey, E. Thomsen, G. Graff, P. Balducci, M. Kintner-Meyer, and V. Sprenkle, *J. Power Sources*, **247**, 1040 (2014).
30. J. S. Newman and C. W. Tobias, *J. Electrochem. Soc.*, **109**(12), 1183 (1962).
31. L. F. Arenas, C. Ponce de León, and F. C. Walsh, *J. Energy Storage*, **11**, 119 (2017).
32. P. Vanysek, in *CRC Handbook Chem. Phys.*, 98th ed., J. R. Rumble, Editor, p. 5–74, Taylor & Francis Group, Boca Raton, FL (2018).
33. Y. Chou, Z. Y. Siao, Y. F. Chen, L. Y. Sung, W. M. Yang, and C. C. Wang, *J. Power Sources*, **195**(2), 536 (2010).
34. Q. Chen, M. R. Gerhardt, L. Hartle, and M. J. Aziz, *J. Electrochem. Soc.*, **163**(1), A5010 (2015).
35. J. D. Milshtein, K. M. Tenny, J. L. Barton, J. Drake, R. M. Darling, and F. R. Brushett, *J. Electrochem. Soc.*, **164**(11), E3265 (2017).

Supplemental Information

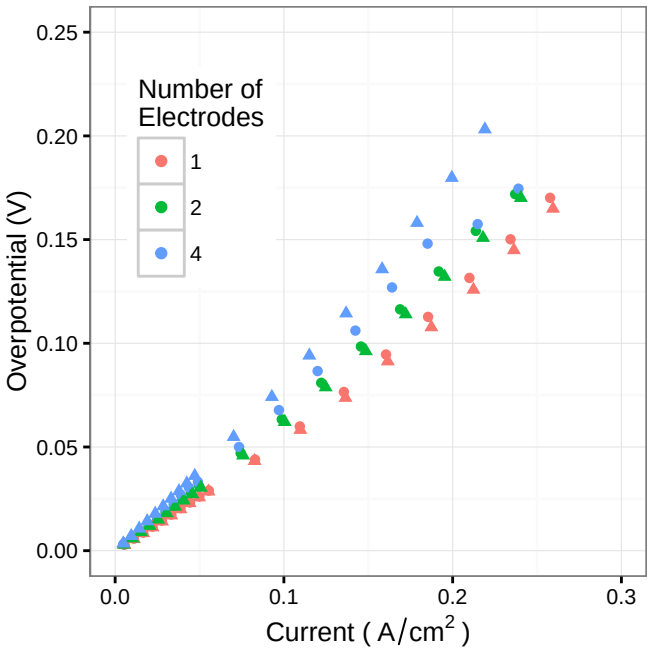

Figure S1: Effect of increasing electrode thickness on single-reservoir cell performance. The "wide channel" flow field was used (1.59 mm channel width, 0.79 mm land width). Stacks of 1, 2, or 4 electrode sheets were used, with 0.008 inches of PTFE gasket thickness per electrode sheet. Two cell runs for each electrode thickness are shown. Circles represent the first run, and triangles represent the second. Electrolytes were circulated at approximately 120 mL/min. The Nafion membranes used in this experiment were pretreated by soaking in 1 M KCl for 24 hours.

Computational methods

All computations were performed using COMSOL 5.2a.

Fitting of a and k_0

Polarization curves were simulated with a range of values for specific surface area a and electrochemical rate constant k_0. These simulations were compared to the experimental results in Section 4.1 by computing the sum of absolute error (E_{abs}) and the sum of squared error (E_{sq}). The error here is defined as the difference between computed and observed current density at each measured

voltage:

$$E_{abs} = \sum_i |V_{exp}(i) - V_{model}(i)| \tag{35}$$

$$E_{sq} = \sum_i \left(V_{exp}(i) - V_{model}(i)\right)^2 \tag{36}$$

We found that both E_{abs} and E_{sq} are minimized by setting a equal to $40\,\mathrm{cm}^{-1}$ and k_0 to $0.1\,\mathrm{cm/s}$. These errors are reported for a range of a and k_0 values in Figure S3.

Meshing and modeling the two-dimensional electrochemical model

The model was constrained to have elements of a fixed, small length, equal to $(W_C + W_L)/100$, along the electrode-membrane boundary and along the top of each land. Furthermore, the maximum element size was restricted to 1/4 of the electrode thickness throughout the porous electrode domain. Three thin boundary layers were applied to the no-slip boundaries within the porous electrode. A triangular mesh was automatically generated to fill the remainder of the model. Less than 1% variation was found in the computed overpotential when the element size varied from 1/3 to 1/6 of the electrode thickness, and less than 0.5% difference was found when the maximum element size along both the electrode-membrane and electrode-land interfaces was decreased from $(W_C + W_L)/50$ to $(W_C + W_L)/500$.

Meshing the three-dimensional fluid model

In the three-dimensional CFD model, a quadrilateral mesh was constructed on the inlet face of the model with a prescribed maximum element size. Boundary layers consisting of eight layers of thin mesh elements were applied to the side walls of the channel, the top of the land, and the top of the electrode, where no-slip boundary conditions are also enforced. The calculated pressure varied by less than 5% upon decreasing the element size from 1/3 of the electrode thickness to 1/8 of the electrode thickness. This error is within our error estimates for pumping efficiency and electrolyte viscosity. Therefore, element sizes of 1/3 of the electrode thickness were used, to save on computation time.

This two-dimensional quadrilateral mesh was swept in the third direction (parallel to the channel) and subdivided into equally spaced mesh elements. It was found that the computed pressure varied by less than 1% upon increasing the number of subdivisions along the channel length from 15 to 20.

Meshing and modeling the flow-through field

The "flow-through" flow plate was modeled differently than the other plates. First, because it does not repeat, the symmetric boundary conditions are replaced with no-slip, no-flux, insulating walls. The velocity at the inlet to the porous electrode is set to $\frac{\dot{Q}}{L_C W_C}$.

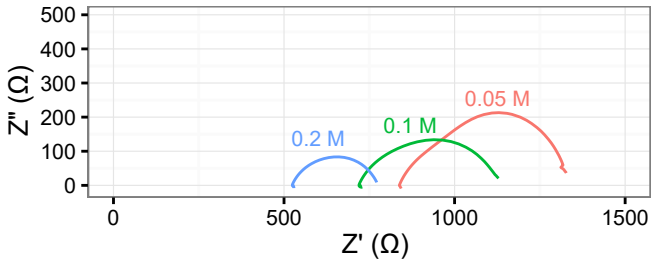

Figure S2: Nyquist plots from galvanostatic electrochemical impedance spectroscopy of a conductivity cell loaded with ferrocyanide-ferricyanide electrolyte at different concentrations. Each electrolyte contained equal amounts of $K_4Fe^{II}(CN)_6$ and $K_3Fe^{III}(CN)_6$ in 1 M KCl. The $K_4Fe^{II}(CN)_6$ concentration of each electrolyte is listed above each curve. High-frequency resistances were calculated by averaging the real component of the impedance in a narrow phase angle range (-0.2 to 0.2 degrees) close to the high-frequency intercept of the real axis. Impedance measurements near the low-frequency intercept (high real impedance) were omitted from this averaging process. These high-frequency resistances were converted to conductivities, which are available in Table 2.

The two-dimensional mesh used for this flow field consisted of quadrilaterals of automatically determined shape and size, with a maximum size equal to 1/8 of the electrode thickness. Furthermore, along the membrane and electrode surfaces, boundary layer meshes consisting of eight thin elements were placed to better approximate the behavior of the fluid near the wall. It was found that there was no variation in computed electrochemical properties when varying the number of mesh elements through the electrode thickness from 8 elements to 16 or varying the number of elements along the length direction from 50 to 400. This mesh was swept in the third direction, along the channel, and subdivided into 20 equally spaced elements to produce the three-dimensional mesh.

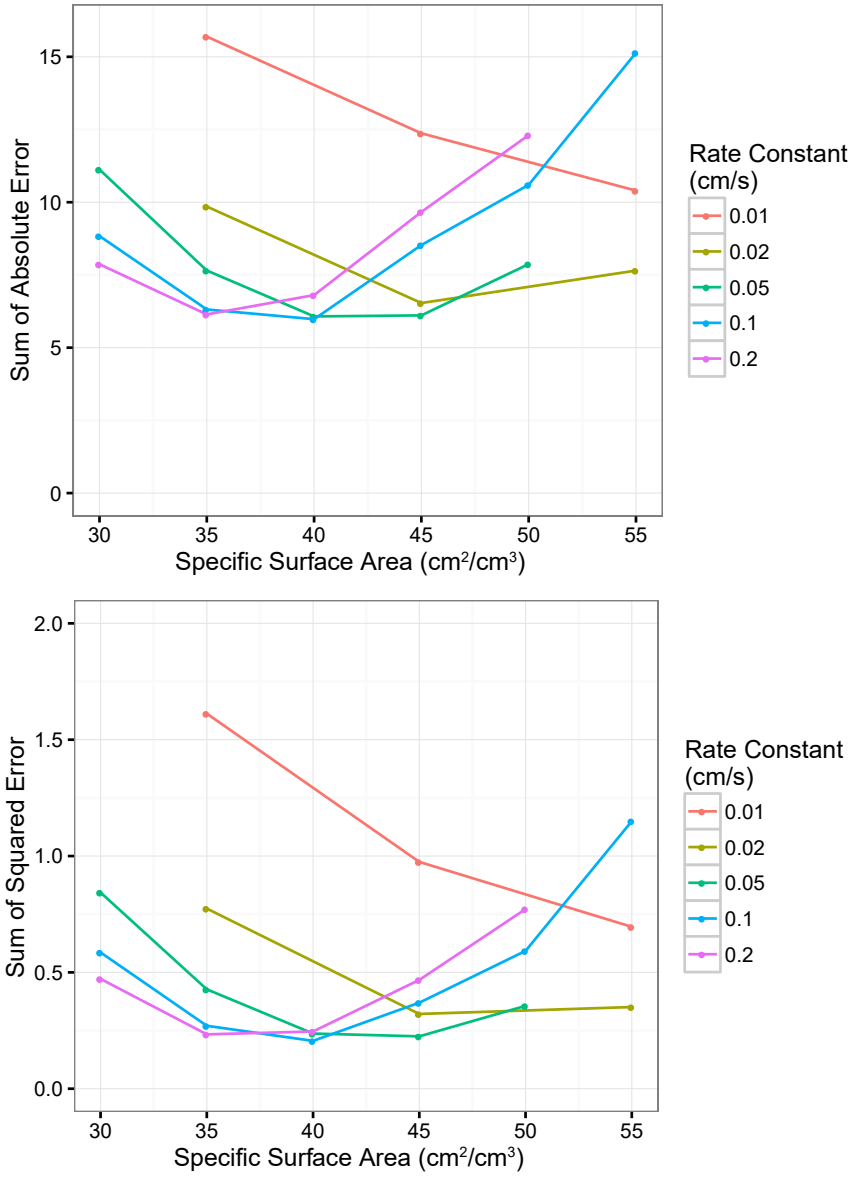

Figure S3: Error from fitting the specific surface area a and electrochemical rate constant k_0. In each case, the error represents the difference between calculated and observed current density at each voltage. The sums of both the absolute error and the squared error are minimized with $a = 40\,\mathrm{cm}^{-1}$ and $k_0 = 0.1\,\mathrm{cm/s}$.